Supplementary Information for

Interfacial Water-Mediated Ion Transport through Electrified Graphene Membranes

The PDF file includes:

Supplementary Note 1. Opportunities and Challenges of Using Nanofluidics Experiments to Probe Interfacial Ion Transport

In stationary systems, ion transport proceeds primarily via two mechanisms: migration, driven by electric potential gradients, and diffusion, driven by chemical potential gradients. While both mechanisms depend on intrinsic properties such as ion mobility and diffusivity, their behaviour is also shaped by extrinsic factors, including the electric field, ionic concentration profiles, and the surrounding solvent environment. Measurements of ionic flux under controlled migration or diffusion conditions offer a powerful, system-level probe of ion–ion, ion–solvent, and ion–interface interactions. This probe is especially sensitive at nanoscopic interfaces, where electrostatic modulations and spatial confinement can amplify subtle interfacial effects. In this context, ion transport experiments that have been widely used in nanofluidics studies serve not only as functional measurements, but also as indirect structural and mechanistic diagnostics, revealing how ions collectively respond to interfacial environments[1–15]. This Note outlines the complementary roles of migration- and diffusion-based measurements in probing interfacial ion transport, the experimental challenges associated with each, and the strategies we developed in this work to overcome these limitations using multilayered graphene membranes.

1.1 Migration-Based Ion Transport as an Effective Tool for Inferring Interfacial Properties

Migration-based measurements, where ion transport is driven by an applied electric field, have become the predominant method for probing interfacial ion transport, especially in nanofluidic systems[1,4–7,12,15]. Their widespread use stems from several practical advantages, including experimental simplicity, robust and quantifiable ionic response, and high sensitivity at small scales. Migration measurements can be readily implemented in standard electrochemical setups, such as two- or three-electrode configurations, which are straightforward to operate and compatible with a wide range of micro- and nanofluidic devices. These techniques also offer exceptional sensitivity, even with a limited population of accessible analytes, an important feature in small-scale nanofluidic systems. Such capabilities have made nanopores and nanoslits benchmark platforms for studying confined interfacial transport.

Beyond enabling direct measurements of ion flux, migration-based experiments have proven especially valuable for inferring interfacial properties of ions, solvents, and their interactions. The measured ionic current reflects the combined effects of ion mobility, concentration, valence, and the local electric field. Although current is not determined by mobility alone, when electrolyte composition, surface charge, and channel dimensions are well controlled and interpreted through appropriate ion transport theories, migration data can be used to extract meaningful interfacial properties, including conductance, permselectivity, surface charge density, and electrostatic screening.

These advantages explain why migration has become the default approach for investigating ion transport involving interfaces. However, it is important to note that applying a bias voltage to perform migration measurements (e.g., current–voltage analysis) inherently perturbs the system, potentially altering the native ion structure at the interface[16–18]. Moreover, as discussed below, migration-based methods capture only a subset of ion transport behaviours, underscoring the need for complementary diffusion-based approaches to achieve a more comprehensive understanding.

1.2 Diffusion Measurement as a Complementary Tool in Probing Interfacial Properties and Its Challenges

Diffusion-based experiments, where ion transport is driven by concentration gradients, avoid the introduction of external potential disturbances to interfacial ion structures, but have been far less frequently employed in studies of ion transport at electrochemical interfaces. A key reason lies in the experimental complexity of tracking ion diffusion, which requires dynamic monitoring of the spatial distribution and chemical identity of ions over time. Unlike migration-based approaches, where ionic currents offer a direct electrical signal, diffusion does not produce a continuous output that can be easily measured in real time. Instead, capturing diffusion behaviour demands either indirect readouts (e.g., conductivity, spectroscopy, or tracer-based methods) or spatially resolved concentration measurements, which are difficult to perform at nanoscopic interfaces with limited ion populations[16]. These technical constraints have made it challenging to isolate interfacial contributions from bulk diffusion, particularly in open or weakly confined systems. Consequently, diffusion-based methods are often underutilised, limiting the ability to probe how interfacial structure, solvent organisation, and short-range interactions influence the collective dynamics of ions under realistic operating conditions.

Another contributing factor is the common assumption that ion diffusivity can be inferred from ionic mobility (typically obtained from migration measurements) using the well-known Nernst–Einstein (N–E) relation:

$$\mu_i = \frac{q_i D_i}{k_\mathrm{B} T}$$

where q_i is the ionic charge, D_i is the diffusivity of the ions, k_B is the Boltzmann constant, and T is the absolute temperature. Under ideal conditions, this relation allows one to estimate diffusivity from mobility measurements, or vice versa, and is frequently applied in electrochemical and transport analyses.

However, the underlying assumptions of the N–E relation are often overlooked, particularly by readers less familiar with ion transport phenomena under realistic conditions. In the classical electrostatic framework, typically valid for dilute bulk solutions, ion transport is dominated by long-range Coulombic interactions, while short-range ion–ion and ion–solvent interactions are assumed negligible. Under these idealized conditions, the relation between mobility and diffusivity holds[16].

In more concentrated or interfacially complex systems, the idealised assumptions underlying the N–E relation break down[16]. At high concentrations, phenomena such as ion–ion correlations, specific ion–solvent interactions, and even ion pairing can occur. For example, neutral ion pairs can contribute to diffusion but not to migration, which disrupts the assumed correlation between measured mobility and diffusivity. A recent study[16] shows that under extreme nanoconfinement, ion diffusion is severely hindered due to restricted ion–water dynamics, while migration remains largely unaffected as the applied electric field disrupts this confinement. This contrast highlights fundamental discrepancies between diffusion and migration, challenging the validity of the N–E relation in confined or concentrated systems. At electrified interfaces, additional complexity arises from spatial variation in dielectric properties[19], interfacial solvent structuring[20], and ion clustering[21–23] These effects cannot be captured by mean-field electrostatics or single-ion mobility measurements alone.

The need to directly measure ion diffusion becomes even more critical when considering the inherently coupled nature of cation and anion transport in electrolyte solutions[24]. Unlike the diffusion of neutral molecules, ionic diffusion must obey the principle of local electroneutrality. In real electrolyte solutions, cations and anions coexist, and their diffusion is electrostatically coupled, meaning they cannot move entirely independently without generating charge separation. If one ionic species diffuses faster than the other, it creates a local imbalance of charge, which in turn induces an internal electric field opposing further separation. This field slows down the faster ion and accelerates the slower one until a dynamic equilibrium is reached. The result is ambipolar diffusion, where the transport of cations and anions becomes interdependent, and the net ionic flux maintains electroneutrality across the system.

In ideal symmetric monovalent electrolytes such as dilute KCl, the effective ambipolar diffusion coefficient $D_{\pm}$ can be expressed using the Nernst–Einstein relation as:

$$D_{\pm} = \frac{2D_{+}D_{-}}{D_{+} + D_{-}}$$

where D_{+} and D_{-} are the diffusion coefficients of cations and anions, respectively[24]. This expression illustrates that even under ideal conditions, the effective diffusion rate is limited by the slower ion. In more complex environments such as confined or interfacially structured systems, deviations from this ideal behaviour are expected due to asymmetries in solvation, charge regulation, or interfacial field effects. For example, our simulations reveal that the lateral self-diffusivities of K^{+} and Cl^{-} ions in graphene nanochannels under different surface charge are indeed reduced compared with their bulk values (**Supplementary Fig. 40**), likely due to cluster formation or surface drag effect[25,26]. These deviations further underscore the importance of directly measuring ambipolar diffusion rather than assuming it can be inferred from mobility-based approaches.

For these reasons, concentration-gradient-driven diffusion experiments, especially those targeting ambipolar transport, offer a valuable complementary approach to migration-based methods. By probing the collective dynamics of cations and anions, diffusion measurements are inherently sensitive to short-range interfacial phenomena such as ion–surface binding, ion–ion correlations, and solvent-mediated interactions. As demonstrated in the main text, our experiments and molecular dynamics simulations reveal pronounced gating asymmetries and voltage-dependent behaviour in ambipolar ion diffusion along graphene interfaces, highlighting the value of this approach in uncovering interfacial transport mechanisms that go beyond classical electrostatic descriptions.

In addition to their mechanistic relevance, ambipolar diffusion processes are central to a wide range of real-world applications including dialysis, nanofiltration, biological ion channels, and electrochemical devices[24]. These systems depend on the collective, electroneutral transport of ions. Gaining experimental insight into how interfacial properties modulate ambipolar diffusion is therefore essential for the design and optimisation of advanced ionic transport technologies.

1.3 Key Considerations in Our Concentration-Gradient-Driven Ion Transport Design

To address the experimental challenges of probing ion transport, particularly ambipolar diffusion across electrified interfaces, we adapted established nanofluidic design principles and introduced several key advancements to enable more robust, interpretable, and scalable measurements.

Amplification of nanochannels and interfaces: A core feature of our approach is the use of multilayered graphene membranes (MGMs), constructed by stacking reduced graphene oxide (rGO) sheets into an ensemble of nanochannels aligned with the ion transport direction. As illustrated in Fig.

1a, each rGO layer offers an atomically thin, ion-accessible interface, and the stacked architecture collectively yields a highly amplified interfacial area. This interface amplification strategy enhances the cumulative ion transport signal, enabling sensitive quantification of diffusion using standard techniques such as ion conductivity meters, inductively coupled plasma and ion chromatography measurements without the need for real-time imaging or specialized probes. Notably, this design is intrinsically compatible with a wide range of electrolyte solutions and does not require buffer systems. This greatly expands the diversity of ions that can be tested, overcoming the limitations of earlier diffusion studies that often relied on fluorescent dyes[16] and were thus restricted to a narrow subset of ionic species. Furthermore, eliminating buffering agents helps avoid potential chemical interferences from buffer-ion interactions reported in previous studies[27].

Minimising the interference of extreme nanoconfinement: Nanofluidic channels offer high surface-to-volume ratios that inherently increase the influence of interfacial interactions and facilitate detection of small ionic fluxes. However, extreme nanoconfinement, typically associated with sub-2 nm slit dimensions, can introduce artifacts that obscure intrinsic interfacial phenomena. These include steric exclusion effects, ion dehydration barriers, and entrance/exit effects that arise when molecular-scale dimensions are comparable to ion or solvent sizes[6]. To mitigate these issues, our design employs relatively large interlayer spacings (~>2 nm) in the MGMs. This approach preserves sufficient confinement to probe interfacial transport phenomena while largely avoiding the complications associated with extreme nanoconfinement (in combination with the cross-validation strategy described in the following), thereby ensuring that observed behaviours reflect genuine interfacial ion dynamics rather than confinement-induced artefacts[28].

Cross-validation through systematic experimental design: As discussed in the main text, resolving ion dynamics under non-equilibrium conditions at electrified interfaces remains experimentally challenging, and each measurement technique carries inherent strengths and limitations. Moreover, unlike single nanochannels with well-defined geometries, MGMs feature a more complex internal architecture that can complicate mechanistic interpretation. To ensure the generality and reproducibility of our findings, we implemented a comprehensive suite of cross-check experiments, systematically varying interlayer spacing, electrolyte concentration, ion type, and gating voltage (including polarity). We further combined diffusion- and migration-based measurements under matched conditions and employed alternative device configurations to isolate specific transport behaviours. Importantly, the multilayered structure enables ion transport to be examined across a wide voltage range, supporting direct comparisons and detailed analysis of voltage-gated asymmetries.

These strategies collectively affirm that our observations reflect intrinsic interfacial ion transport mechanisms rather than artefacts arising from membrane architecture or spatial confinement.

Complementarity with theoretical simulation: Due to the inherently multiscale nature of interfacial ion transport, spanning atomic-scale interactions to mesoscopic fluxes, both experimental characterization and computational modelling face considerable challenges. In many cases, neither approach alone is sufficient to capture the full complexity of ion behaviour across scales[29]. In this study, the use of MGMs provided a relatively simple and structurally well-defined platform that facilitated the construction of tractable models for both continuum and molecular dynamics (MD) simulations. These simplified yet representative configurations allow for meaningful comparisons between experimental results and theoretical predictions, bridging length scales and validating mechanistic interpretations. The ability to achieve such complementarity was key to uncovering the role of interfacial water structuring and dynamic ion clustering in voltage-gated ambipolar transport, phenomena that would be difficult to access through either simulations or experiments alone.

Supplementary Note 2. Continuum Modelling of Ion Diffusion Through Charged Graphene Channels

2.1 Justification of using ion correlations to modify the Poisson-Nernst-Planck theory

Given the experimentally observed enhancement of ambipolar ion diffusion at highly electrified interfaces, an effect that could not be captured by the classical PNP model, it was necessary to adopt a more advanced theoretical framework to explain this unexpected phenomenon. The classical PNP theory is fundamentally based on the assumptions of dilute electrolyte solutions containing point-like ions interacting with low-charge surfaces, where only long-range mean-field electrostatics are considered.[30] However, in systems with high surface charge densities, elevated applied voltages, and locally concentrated ionic environments, such as those examined in this study, short-range Coulombic interactions and ion–ion correlations can become significant, leading to deviations from classical predictions. Among various efforts in modifying classical PNP model, Bazant et al. proposed a modified mean-field theory by introducing a non-local dielectric response term with only one additional parameter, ion correlation length l_c.[21] This simple mathematical framework has been previously used to predict several macroscale non-classical ion distributions such as overscreening and charge inversion, where the counter-ion and co-ion concentration profiles oscillate[21], markedly differing from the monotonic profiles predicted by classical PNP theory. Additionally, the modified model has predicted anomalous water transport in highly charged interfacial regions, including electro-osmosis flow reversal.[31]

With this ion correlation modified PNP model (denoted as IC/PNP), we were able to capture the experimentally observed enhancement of ambipolar ion diffusion at negatively charged nanochannels (**Supplementary Fig. 17**). Moreover, the IC/PNP model also predicted higher D_{KCl} values at lower feed solution concentrations and in narrower nanochannels (**Supplementary Fig. 18**), both of which are consistent with the experimentally observed trends.

2.2 The diffusive and electrophoretic components of the ion permeation flux

In conventional low-charge systems, ion permeation driven by concentration gradients is typically dominated by diffusion flux, with migration flux contributions considered negligible. However, at highly electrified interfaces such as those studied here, this assumption no longer holds. Our simulations reveal that under negative surface charges, where K^+ acts as the counter-ion and Cl^- as the co-ion, the accumulation of counter-ions at the channel walls leads to a highly non-uniform distribution of co-ions along the transverse direction (**Supplementary Fig. 19**). This enriched and spatially heterogeneous ion environment creates significant lateral variations in co-ion concentrations, which in turn induces a lateral electric potential gradient across the channel slit (**Supplementary Fig. 20**). This emergent potential gradient gives rise to a distinct migration flux component that supplements the classical diffusion flux during concentration-driven permeation (**Supplementary Fig. 21**). This mechanism represents a marked departure from the traditional diffusion-only paradigm. Quantitatively, at a low surface charge density (-0.022 C m^{-2}), diffusion remains dominant, contributing ~97% of the co-ion permeation flux (**Supplementary Fig. 22**), with migration accounting for only ~3%. However, at a high charge density (-0.09 C m^{-2}), this balance shifts dramatically, with migration flux contributing ~60% of the co-ion flux. Similar trends were observed across different channel sizes and feed concentrations (**Supplementary Figs. 23 and 24**). These findings highlight a charge density-dependent transition in the dominant transport mechanism—from diffusion-dominated permeation at low charge densities to migration-dominated permeation at high charge densities. This electrification-driven mechanism introduces a non-classical mode of ion permeation along charged interfaces, underscoring the need to account for migration flux when interpreting concentration-driven ion transport in such systems.

2.3 The role of interfacial region in the ion transport through charged graphene channels

To elucidate the contribution of electrified interfacial regions to the observed enhancement of ion diffusion, we analysed the spatial distribution of ion permeation flux along the transverse direction of graphene channels. Simulations were conducted across nanochannels with slit sizes ranging from 2.5 to 5.0 nm and under feed concentrations from 50 to 1000 mM. As shown in **Supplementary Fig. 25**, for all channel sizes, the ion flux consistently reaches its maximum at approximately 1.2 nm from the channel wall, indicating that ion transport is predominantly confined to the near-surface interfacial regions. With increasing channel size, the flux distribution becomes increasingly symmetric, forming two pronounced peaks adjacent to each wall. This observation highlights that the enhanced ion diffusion primarily originates from the electrified interfaces, and that reducing the channel size proportionally increases the contribution of these interfacial regions by increasing the interfacial-to-bulk area ratio. This geometric effect explains the observed D_{KCl} enhancement in narrower channels. Further analysis of flux profiles in 5.0 nm channels at varying feed concentrations (**Supplementary Fig. 26**) provided additional insights. At higher feed concentrations, the peak ion flux shifts closer to the channel surface while its normalised peak value decreases, reflecting a higher absolute permeation flux but a reduced enhancement ratio. This trend highlights that while higher concentrations increase total flux, they also diminish the dominance of the interfacial contribution due to stronger screening effects. Collectively, these findings demonstrate that the enhancement of ambipolar ion diffusion along charged graphene surfaces is governed by the electrified interfacial regions and does not strictly require extreme nanoconfinement. These findings are consistent with our experimental observations of more significant diffusion enhancement in lower feed concentrations and multilayered graphene membranes with smaller sizes.

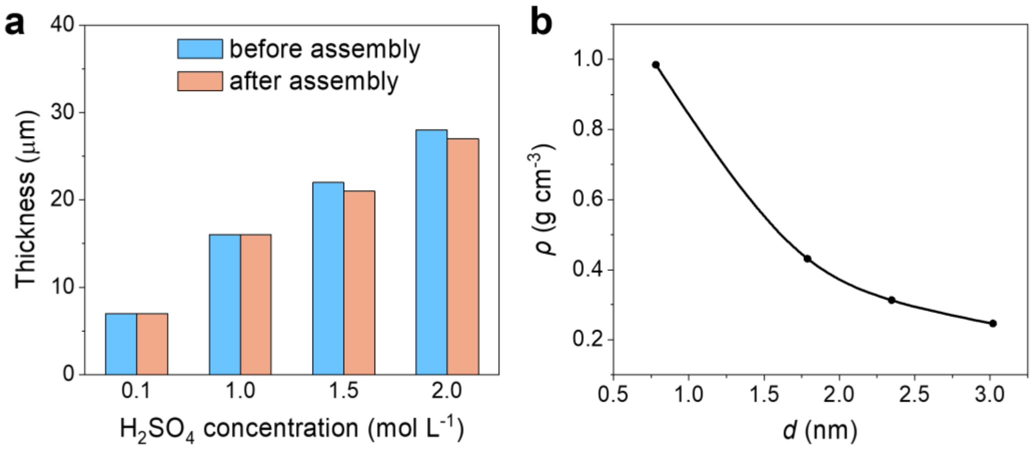

Supplementary Fig. 1 Parameters including thickness, average interlayer spacing, and packing density of as-prepared MGMs. a, Thicknesses of MGMs prepared from varying concentrations of H_2SO_4 solutions and the thickness change before and after measurement on the home-designed ion transport setup. **b**, Estimated average interlayer spacing (*d*) and corresponding packing density (*ρ*) of MGMs.

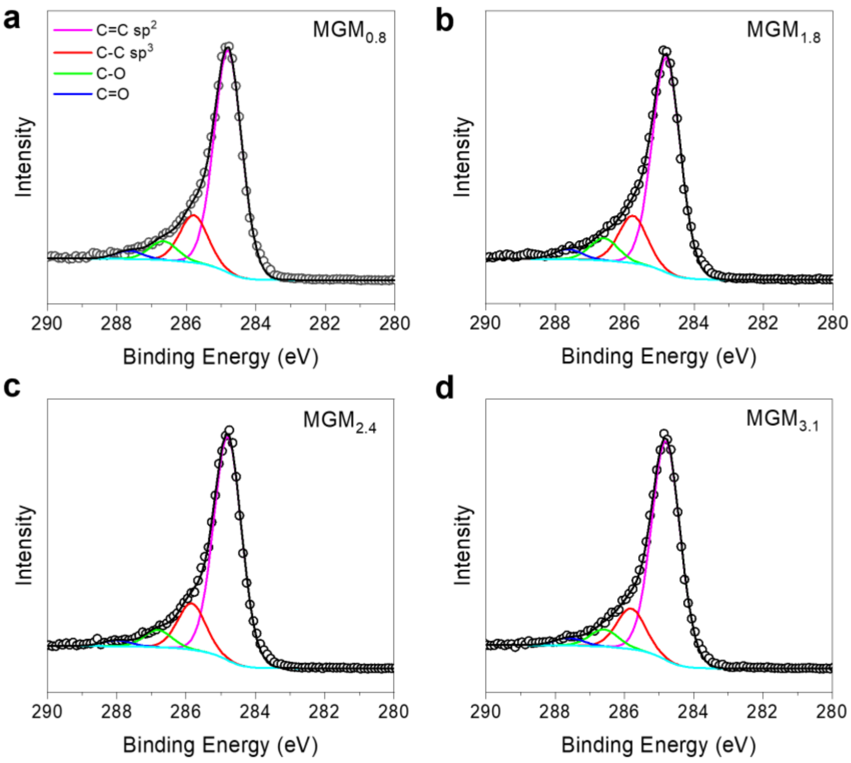

Supplementary Fig. 2 Surface chemistry of MGMs based on XPS measurement. a-d, High resolution C 1s spectra of MGMs with different *d*. These results suggest the presence of negatively charged oxygen-containing groups on rGO sheet of all MGMs, such as hydroxyl and carboxyl groups.

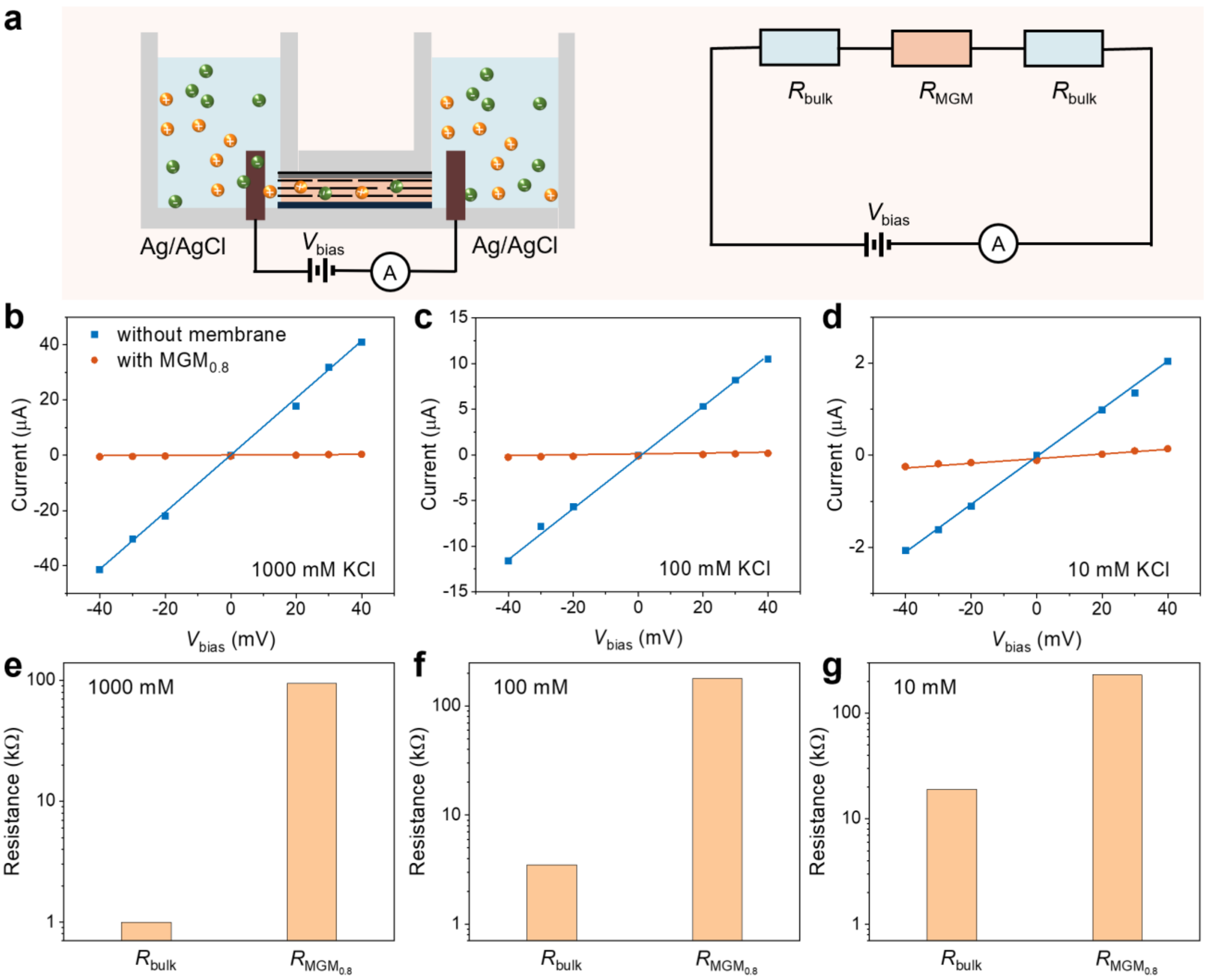

Supplementary Fig. 3 Ionic resistance in the setup with edge planes of MGMs exposed to electrolytes. a, Schematic of the setup configuration and corresponding electric circuit for analysing the composition of measured ionic resistance from *I-V* technique. R_{bulk} and R_{MGM} are the ionic resistance from bulk solutions and assembled membranes, respectively. **b-d**, *I-V* responses for KCl solutions with varying concentrations (10, 100, and 1000 mM) in the setups assembled with and without MGM$_{0.8}$. Dot points are the experimentally measured data, and solid lines are the corresponding linear fittings. **e-g**, The comparison between ionic resistance from bulk solution and membranes for different concentrations of KCl solutions. When the length of membrane used in the designed setup is greater than 4 mm, it was found that the ionic resistance through the membrane significantly exceeded the bulk solution resistance, with a major contribution (92% in 10 mM KCl and 98% in higher concentrations of 100 and 1000 mM) to the measured ionic resistance from ion migration in membranes, ensuring the successful and reliable ion conductance measurements.

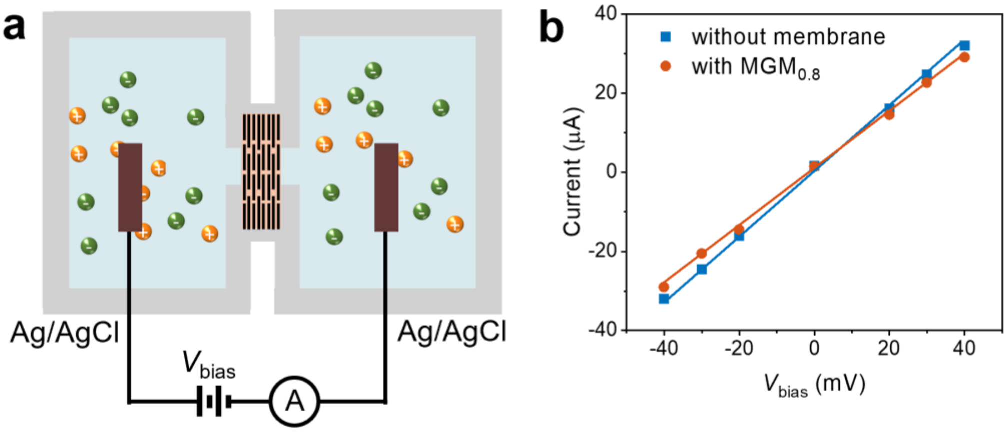

Supplementary Fig. 4 Ionic resistance in the setup with basal planes of MGMs exposed to electrolytes. a, Schematic of the setup configuration used in our previous work[32], where the basal planes of the membrane are exposed to electrolytes. **b**, *I*-*V* responses for 1000 mM KCl solution based on the setup assembled with and without $\text{MGM}_{0.8}$. In this case, the measured ionic resistance is overwhelmed by the bulk electrolyte solution. As a result, detecting variations of ionic resistance through different MGMs proved to be difficult, failing to determine A_{eff} for the comparison of ion permeation flux among MGMs and the comparison with the benchmark of ion diffusion in bulk solution.

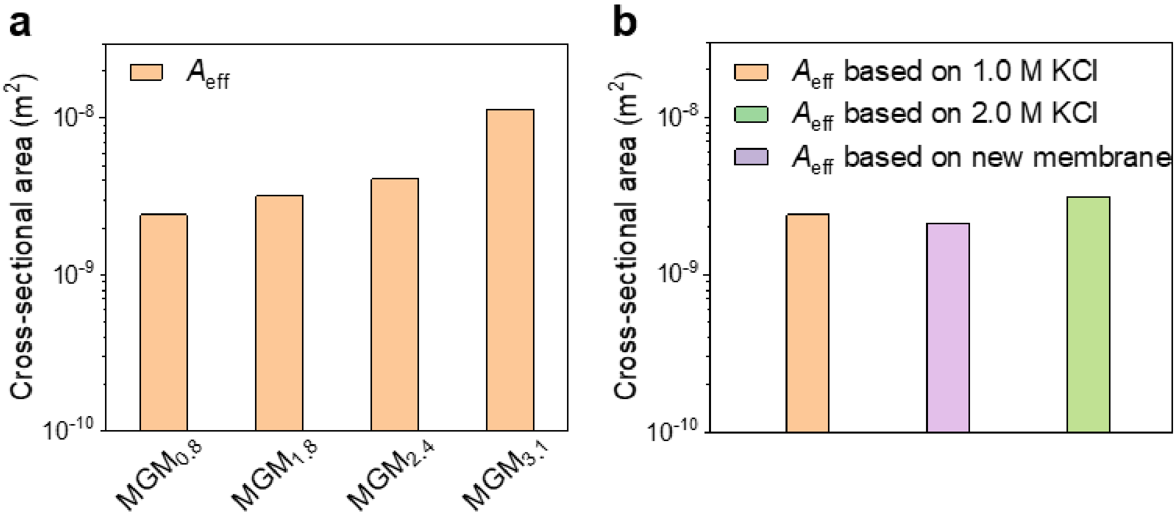

Supplementary Fig. 5 Estimation of the effective cross-sectional area (A_{eff}) for MGMs on the home-designed setup with edge planes of MGMs exposed to electrolytes. a, Estimated A_{eff} for MGMs with various *d* based on the measured ion conductance of a high concentration of 1.0 M KCl solution across membranes. **b**, Cross-check of A_{eff} for $\mathrm{MGM}_{0.8}$ based on the measured ion conductance of a higher concentration of 2.0 M KCl and a new piece of membrane based on the ion conductance of 1.0 M KCl solution.

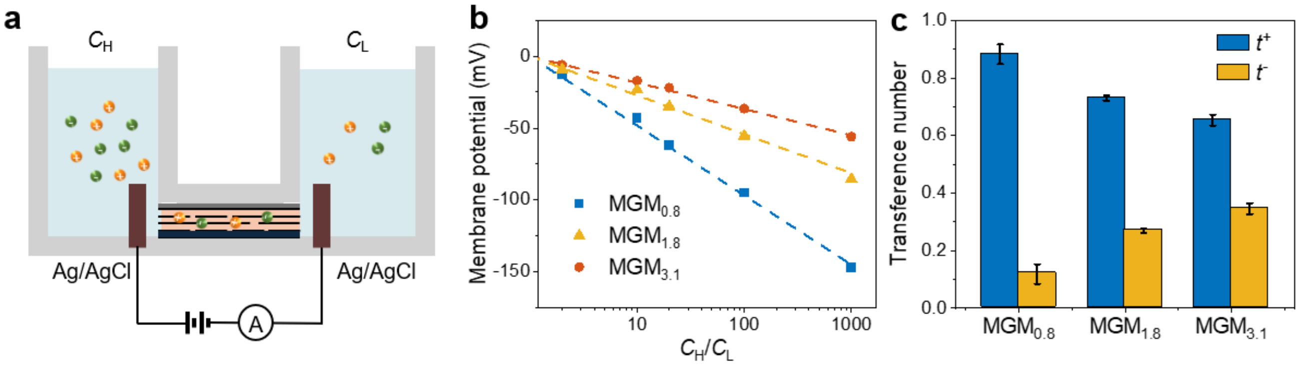

Supplementary Fig. 6 Cation and anion selectivity measurement for three representative MGMs. a, Schematic diagram of the setup filled with KCl solutions of high concentration (C_H) and low concentration (C_L) in the corresponding reservoirs. **b**, Membrane potentials for $\mathrm{MGM}_{0.8}$, $\mathrm{MGM}_{1.8}$, and $\mathrm{MGM}_{3.1}$ with different $C_\mathrm{H}/C_\mathrm{L}$, where C_H was fixed to be 1000 mM and C_L was changed from 1000 to 100, 50, 10, and 1 mM. Dashed lines are the linearly fitted lines based on the experimental data (dot points). **c**, Transference numbers for cation (t^+) and anion (t^-) calculated based on the methods widely used in nanofluidics[6].

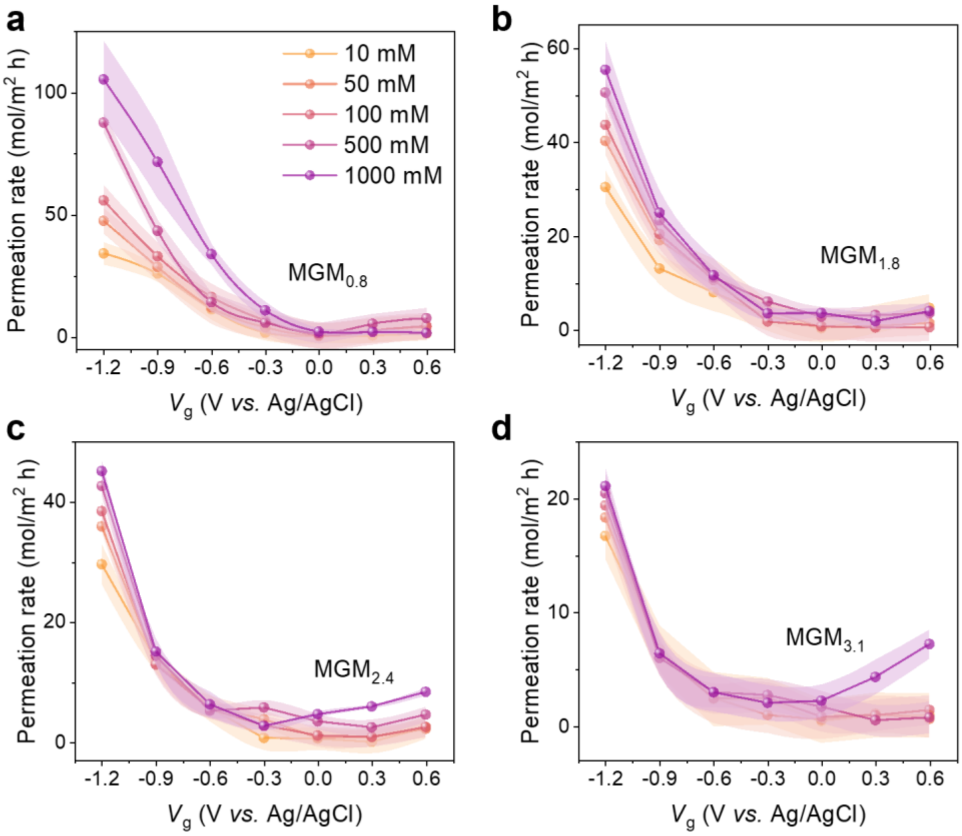

Supplementary Fig. 7 Permeation rates of KCl solution with various concentrations through electrified MGMs with different *d*. **a**, MGM$_{0.8}$, **b**, MGM$_{1.8}$, **c**, MGM$_{2.4}$, and **d**, MGM$_{3.1}$.

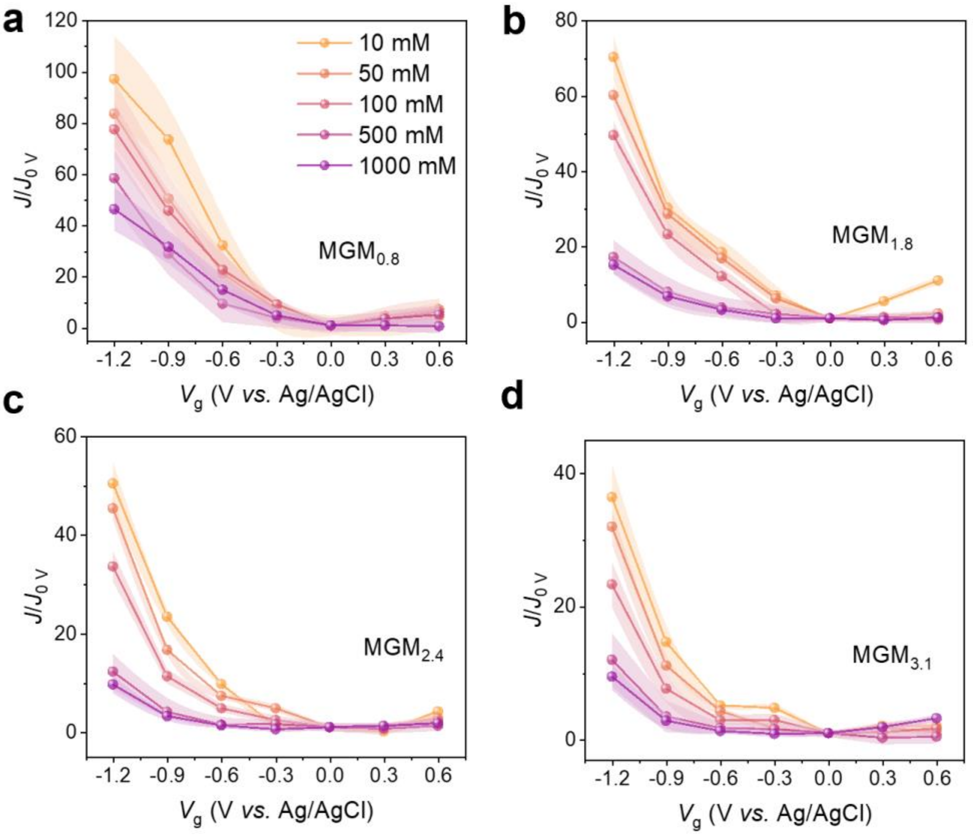

Supplementary Fig. 8 Modulation ratio of permeation rates of KCl solution with varying concentrations through electrified MGMs. a, MGM$_{0.8}$, **b**, MGM$_{1.8}$, **c**, MGM$_{2.4}$, and **d**, MGM$_{3.1}$. To compare the modulation ratio, the permeation rates at various V_g are normalised by the corresponding permeation rates at V_g of 0 V.

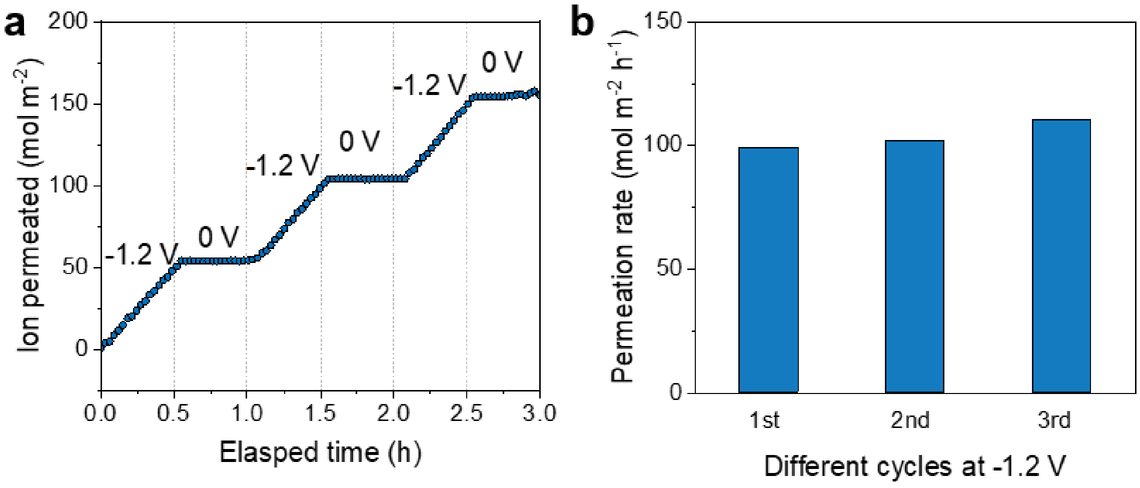

Supplementary Fig. 9 Demonstration of reversible modulation of ion permeation by external V_g. a, 1000 mM KCl diffusion through electrified MGM$_{0.8}$ under the programmed V_g between -1.2 and 0 V for three cycles. **b**, Permeation rates at V_g of -1.2 V in different cycles.

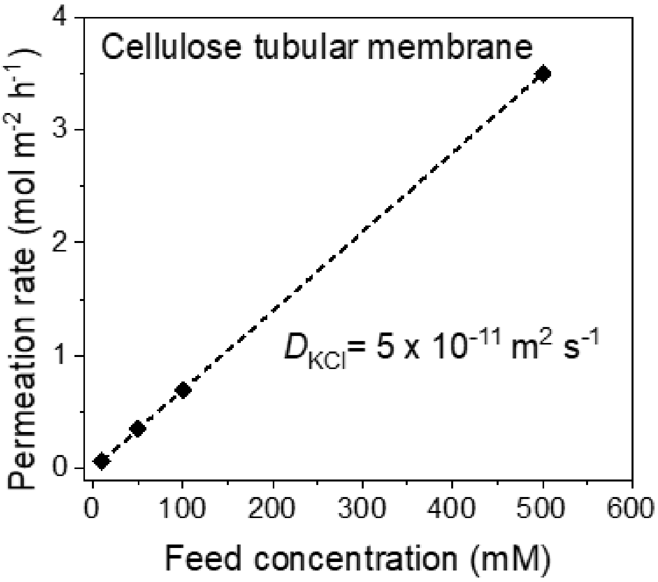

Supplementary Fig. 10 Permeation rates of KCl solution diffusion with various concentrations through commercial cellulose tubular membrane. The linear dependency of permeation rates on feed concentration indicates Fickian diffusion behaviour. The D_{KCl} is calculated to be 5×10^{-11} m^2 s^{-1}.

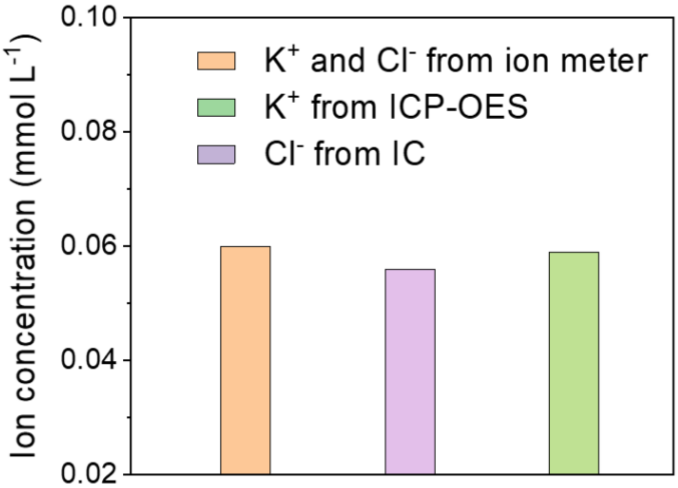

Supplementary Fig. 11 Quantification of ion concentration in permeation reservoir with different techniques including ion meter, inductively coupled plasma optical emission spectrophotometer (ICP-OES), and ion chromatography (IC). For ICP-OES and IC measurements, 3 mL of permeation solution was taken out after the ion permeation test at -1.2 V for 1 h. 1.5 mL was injected to ICP-OES for quantifying the amount of K$^+$ and another 1.5 mL was injected to IC for quantifying the amount of Cl$^-$.

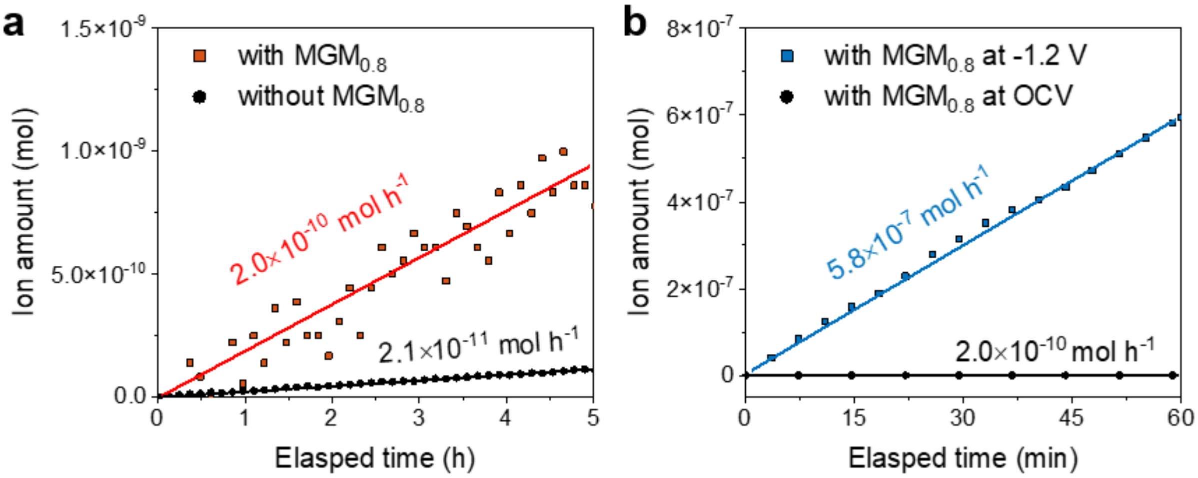

Supplementary Fig. 12 Analysis on the contribution of ion leakage to the measured ion permeation rate. a, Comparison of the amount of ions permeated through the setup assembled without MGM (black curve) and with $MGM_{0.8}$ at OCV (red curve). **b**, Comparison of the amount of ions permeated through the setup assembled with $MGM_{0.8}$ at OCV (black curve) and at -1.2 V (blue curve). Dot points are the experimental data, and solid lines are linear fittings for the calculation of ion permeation rate. The number of ions permeated without membrane was observed to be one order of magnitude lower than that with membrane under OCV and three orders of magnitude lower than that electrified membrane at -1.2 V, suggesting the negligible contribution of leaked ions to ion permeation flux.

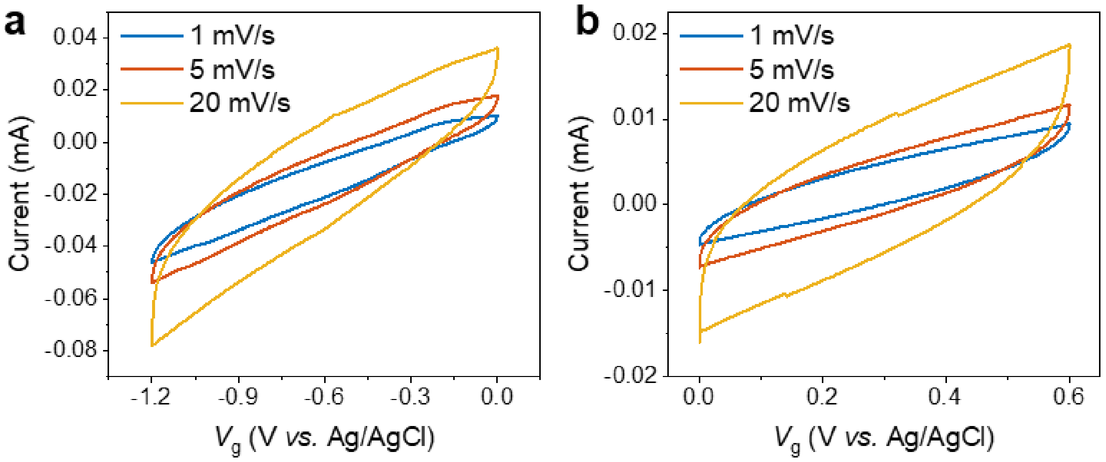

Supplementary Fig. 13 Examining the voltage window without chemical reactions on the diffusion setup. a-b, Cyclic voltammetry curves for $MGM_{0.8}$ at scanning rates of 1, 5, and 20 mV s^{-1} in 1000 mM KCl for voltage window (**a**) from 0 to -1.2 V, and (**b**) from 0 to 0.6 V. CV curves in the examined voltage window did not exhibit any noticeable redox peaks, regardless of the scanning rates from 1 to 20 mV s^{-1}, indicating no detectable chemical reactions within the examined voltage range.

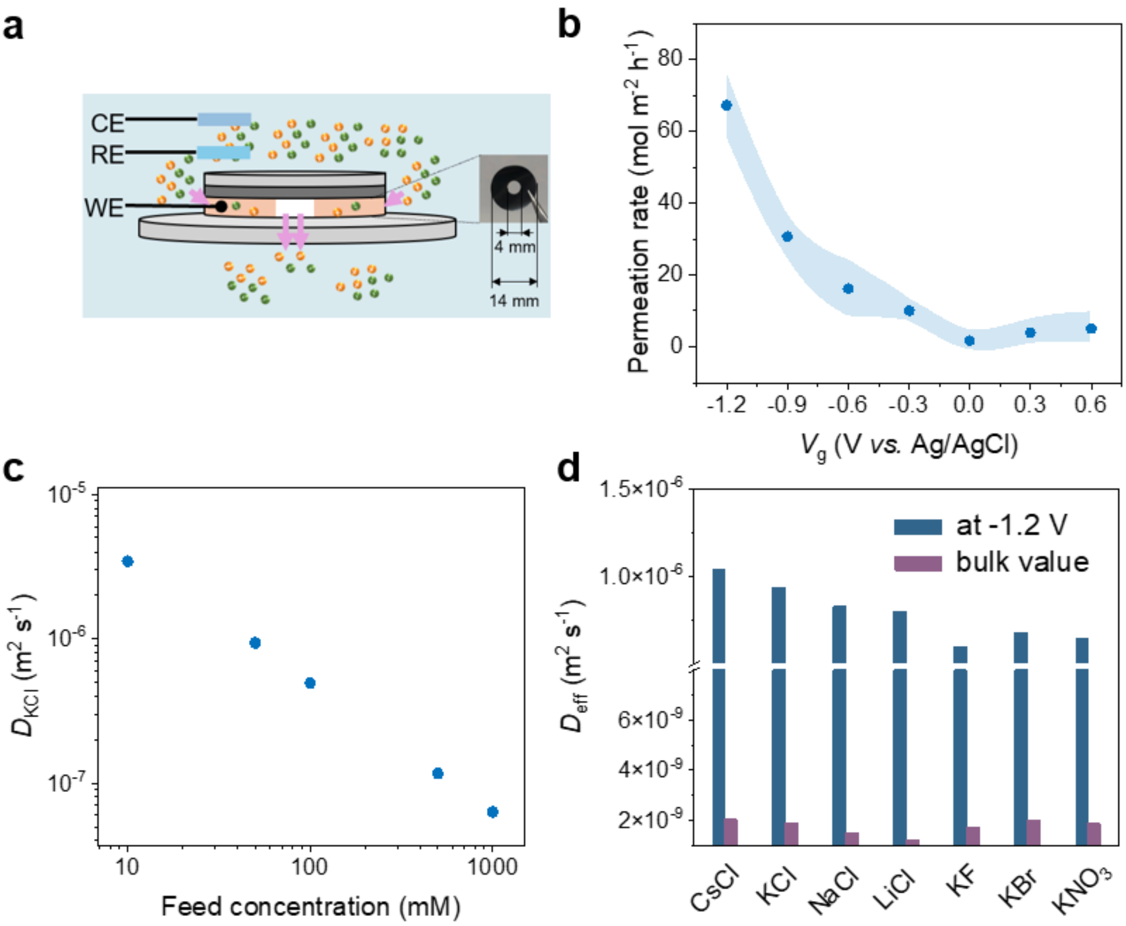

Supplementary Fig. 14 Ambipolar ion diffusion on another home-designed setup with an annular geometry. a, Schematic of another home-designed setup with an annular geometry**.** The inner and outer diameter of annulus membrane is 4 and 14 mm, respectively. **b**, Voltage-dependent permeation rate for 50 mM KCl through MGM$_{0.8}$. **c**, The calculated D_{KCl} for different concentrations of electrolytes. **d**, The calculated effective diffusion coefficient (D_{eff}) for 50 mM of different electrolytes. The MGM was tailored to match this annular configuration, featuring dimensions of 4 mm in inner diameter and 14 mm in outer diameter. This setup offered an effective diffusion length of 2.5 mm, comparable to that of the above rectangle-shaped configuration. The asymmetric response of ion permeation flux to the applied voltage can also be observed. The feed concentration-dependent effective diffusion coefficient exhibited a similar trend to that observed in the rectangle-shaped setup. In particular, for 50 mM KCl diffusion through the electrified MGM$_{0.8}$ at -1.2 V, the effective diffusion coefficient was measured to be 9.8×10^{-7} m^2 s^{-1}, which aligns with the value of 8.0×10^{-7} m^2 s^{-1} obtained in the rectangle-shaped setup. Moreover, the ultrahigh effective diffusion coefficients for various electrolytes including LiCl, NaCl, CsCl, KF, KBr, and KNO$_3$ can also be obtained on the annulus-shaped setup.

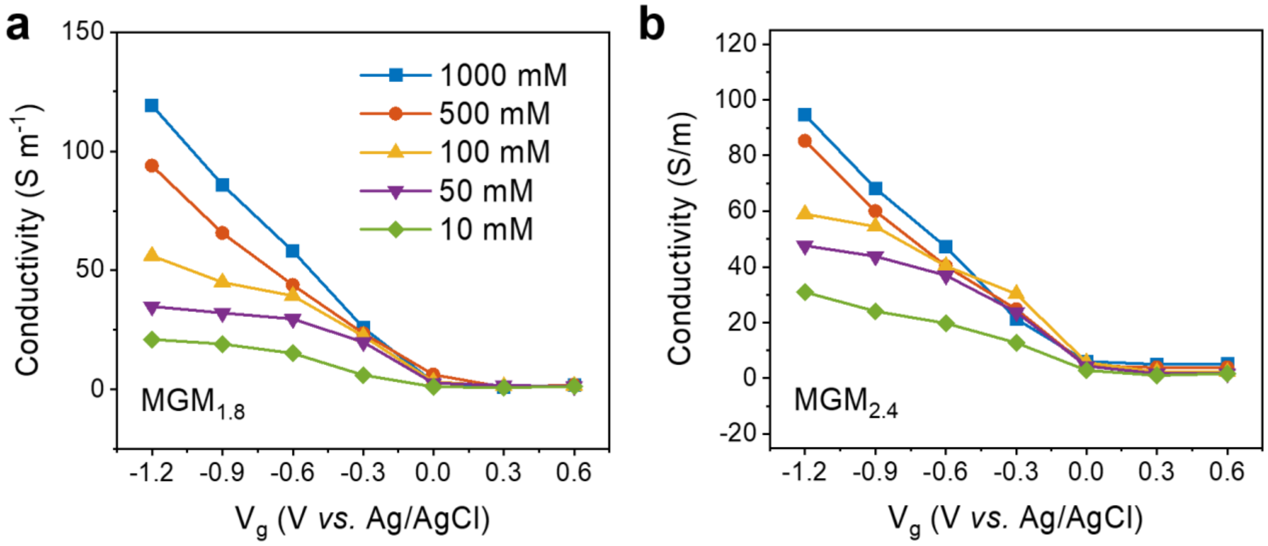

Supplementary Fig. 15 Probing ionic conductivity induced by electrification on MGMs. a-b, Ionic conductivity across electrified MGMs with varied *d* (**a**, MGM$_{1.8}$ and **b**, MGM$_{2.4}$), measured for varying concentrations of KCl solutions.

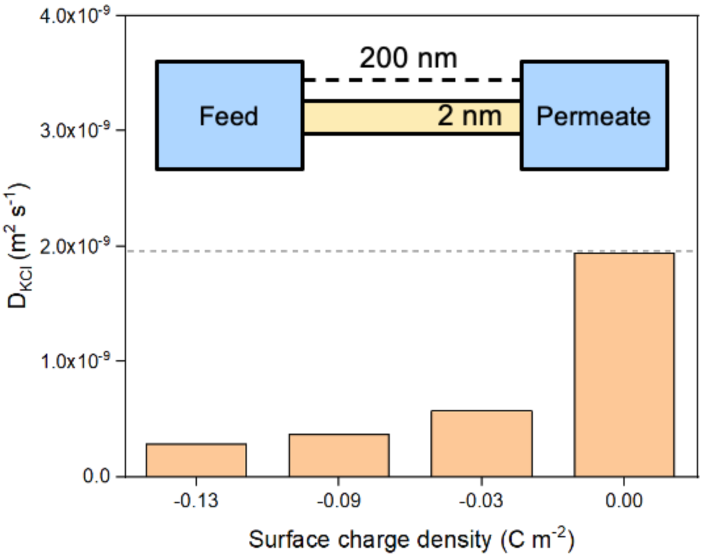

Supplementary Fig. 16 D_{KCl} at various charge densities determined from classical PNP model. The feed concentration is 50 mM KCl and the channel size is 2 nm. The four different charge densities from 0 to -0.13 C m^{-2} correspond to gate voltage at 0, -0.1, -0.2, and -0.3 V, respectively, consistent with the voltages used in IC/PNP model. The grey dashed line indicates the bulk diffusion coefficient of KCl.

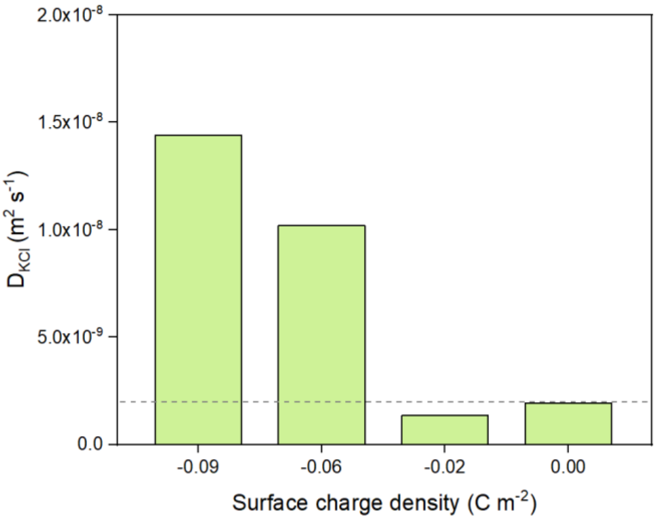

Supplementary Fig. 17 D_{KCl} at various charge densities determined from IC/PNP model. The feed concentration is 50 mM KCl and the channel size is 2 nm. The different four charge densities from 0 to -0.09 C m^{-2} correspond to gate voltage at 0, -0.1, -0.2, and -0.3 V, consistent with the voltages used in classic PNP model. The grey dashed line indicates the bulk diffusion coefficient of KCl. Simulations at higher surface charge densities were limited by numerical instabilities due to the nonlinear coupling in IC/PNP model.

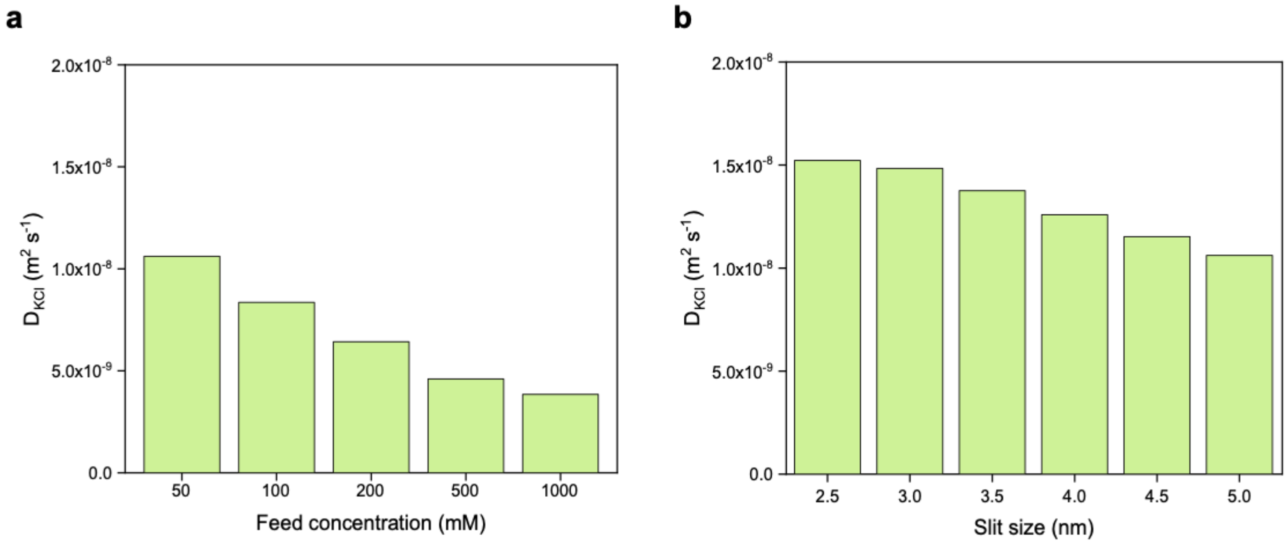

Supplementary Fig. 18 D_{KCl} at various feed reservoir KCl concentration and channel slit size determined from IC/PNP model. The charge densities is -0.09 C m^{-2} correspond to gate voltage at -0.3 V. **a**, D_{KCl} in nanochannels with KCl feed concentration range from 50 to 1000 mM and the channel size is 2.0 nm. **b**, D_{KCl} in nanochannels with channel size range from 2.5 to 5.0 nm, and the KCl feed concentration is 50 mM.

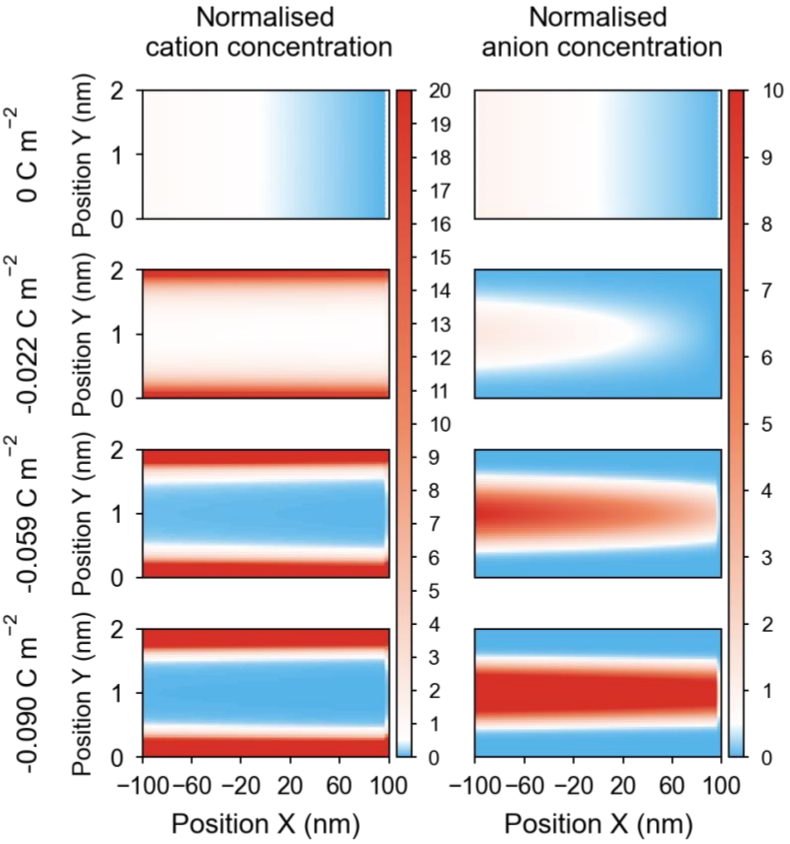

Supplementary Fig. 19 Cation and anion distribution within the 2 nm channel at different charge densities, based on IC/PNP models. The figure presents colour map illustrating the 2D distributions of cation and anion, with concentrations normalised by the feed concentration of 50 mM.

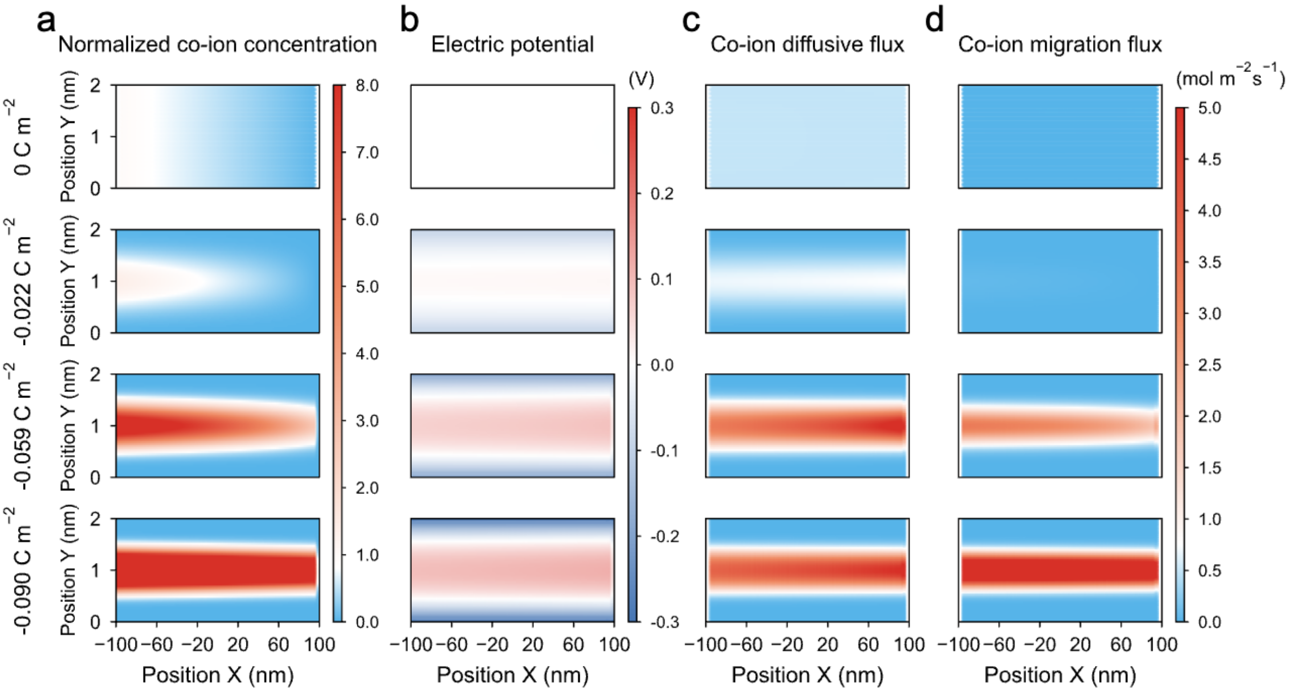

Supplementary Fig. 20 Continuum modelling results of correlated ion transport in 2 nm graphene channels at various charge densities based on IC/PNP theory. a, normalised co-ion (anion) concentration relative to the feed concentration. **b**, electric potential distribution. **c**, anion diffusion flux. **d**, anion migration flux. The IC/PNP results reveal that electrostatic ion correlations lead to co-ion (i.e., anion under negative gating) enrichment near the densely packed counter-ions at the channel surface as surface charge density increases. This co-ion accumulation gives rise to complex ion distributions perpendicular to the channel walls, which, in turn, establish lateral concentration gradients across the slit. These lateral concentration gradients induce a corresponding lateral electric potential gradient, giving rise to an additional flux component, migration flux, that supplements the conventional diffusion flux in concentration-driven ion transport.

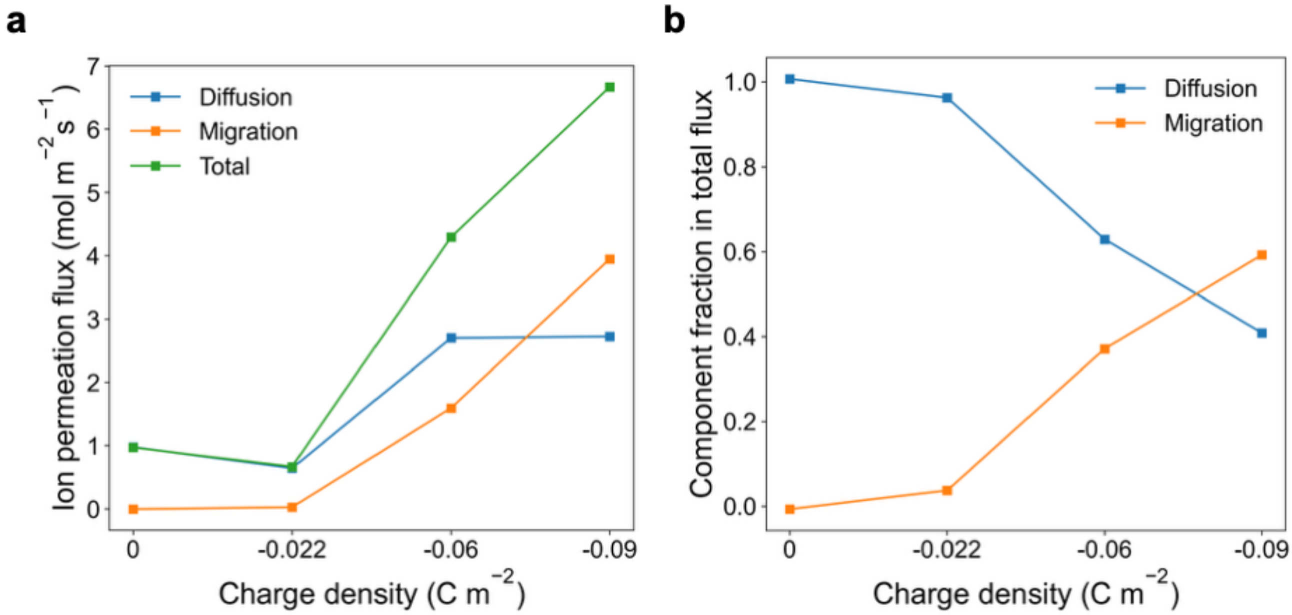

Supplementary Fig. 21 Diffusion and migration components of ion permeation flux across the channels with different sizes. **a**, Diffusion and migration components of ion permeation flux integrated across 2 nm channel at different charge densities. **b**, The factions of diffusion and migration components in total ion permeation flux integrated across 3.5 nm channel at different charge densities. All these results are determined from the results in Supplementary Fig. 20.

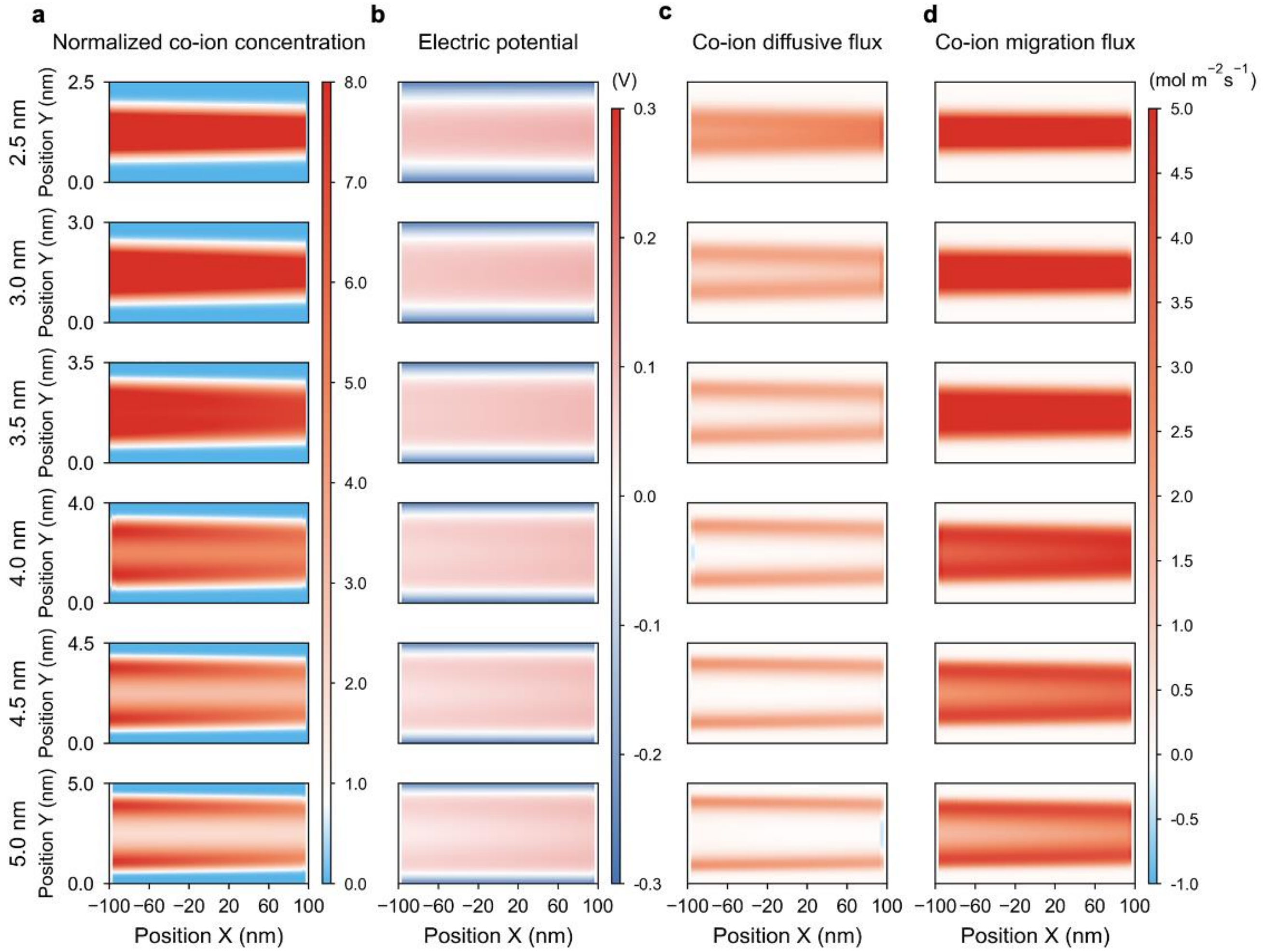

Supplementary Fig. 22 Continuum modelling of 50 mM KCl diffusion through the electrified channels with various sizes at the highest charge density. a-d, Colour map for the 2D distribution of (**a**) anion concentration, (**b**) electric potential, (**c**) anion diffusion flux, and (**d**) anion migration flux.

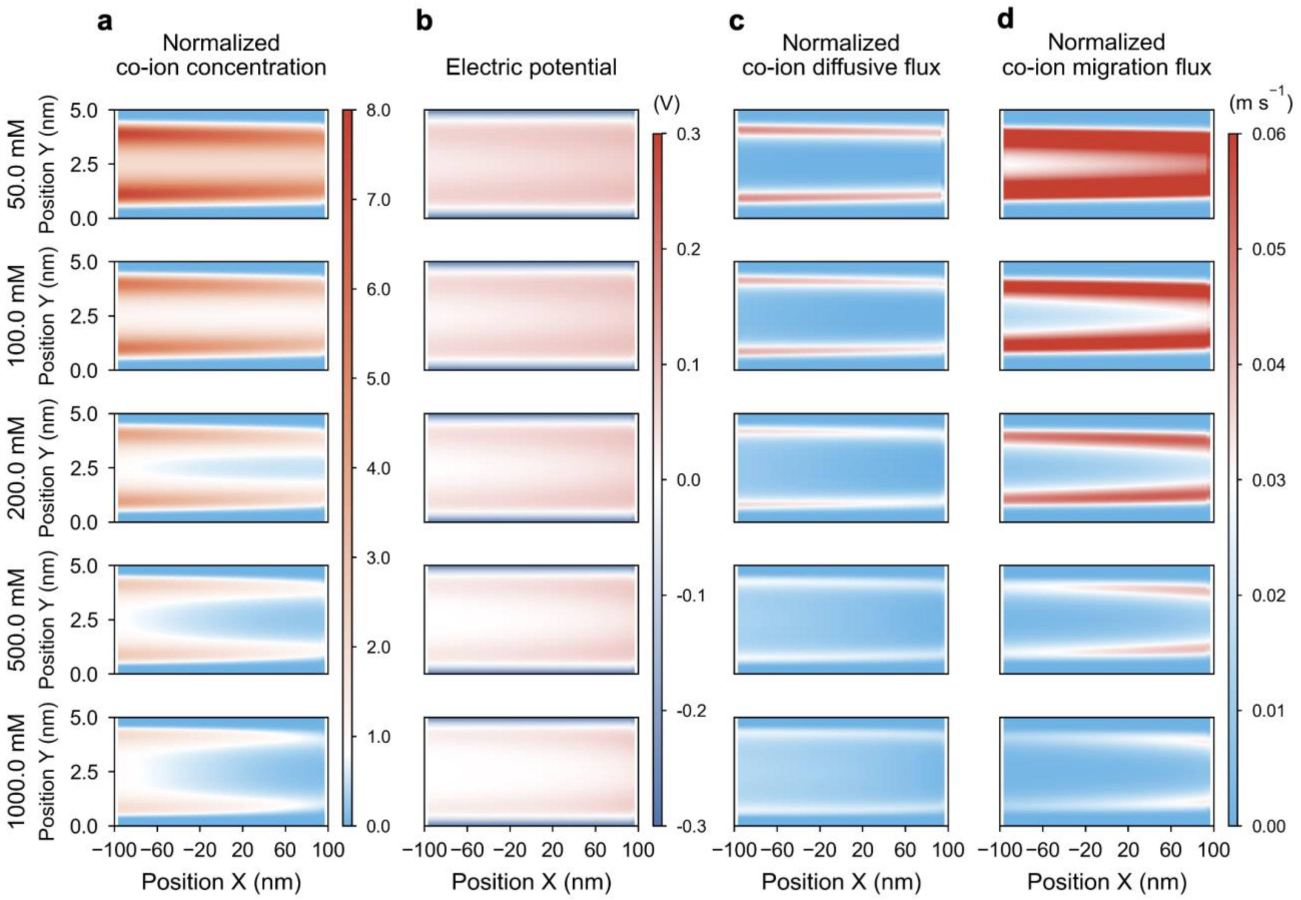

Supplementary Fig. 23 Continuum modelling of KCl diffusion through electrified 5 nm channel with various feed concentrations at the highest charge density. a-d, Colour map for the 2D distribution of (**a**) anion concentration normalised by the corresponding feed concentration, (**b**) electric potential, (**c**) anion diffusion flux normalised by the corresponding feed concentration, and (**d**) anion migration flux normalised by the corresponding feed concentration.

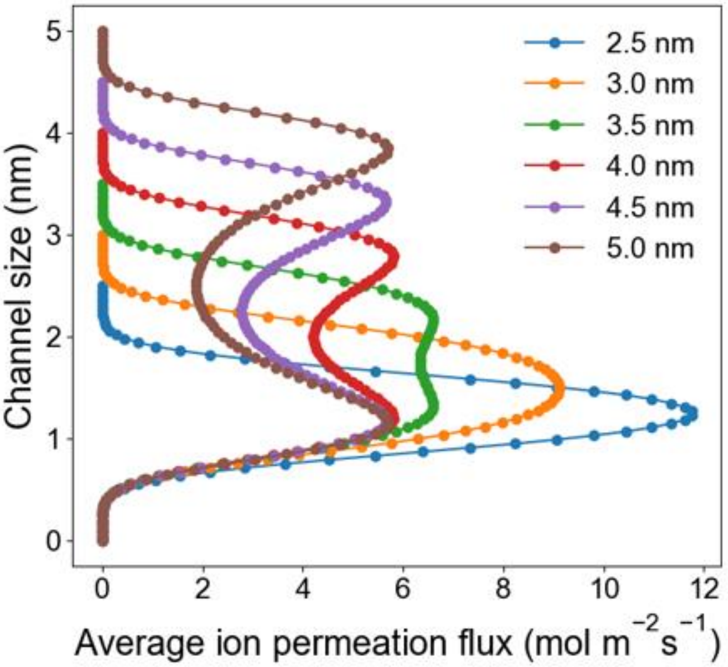

Supplementary Fig. 24 Distribution of ion permeation flux averaged in the lateral direction across the electrified channels with various sizes at the highest charge density. All these results are determined from the results in Supplementary Fig. 22.

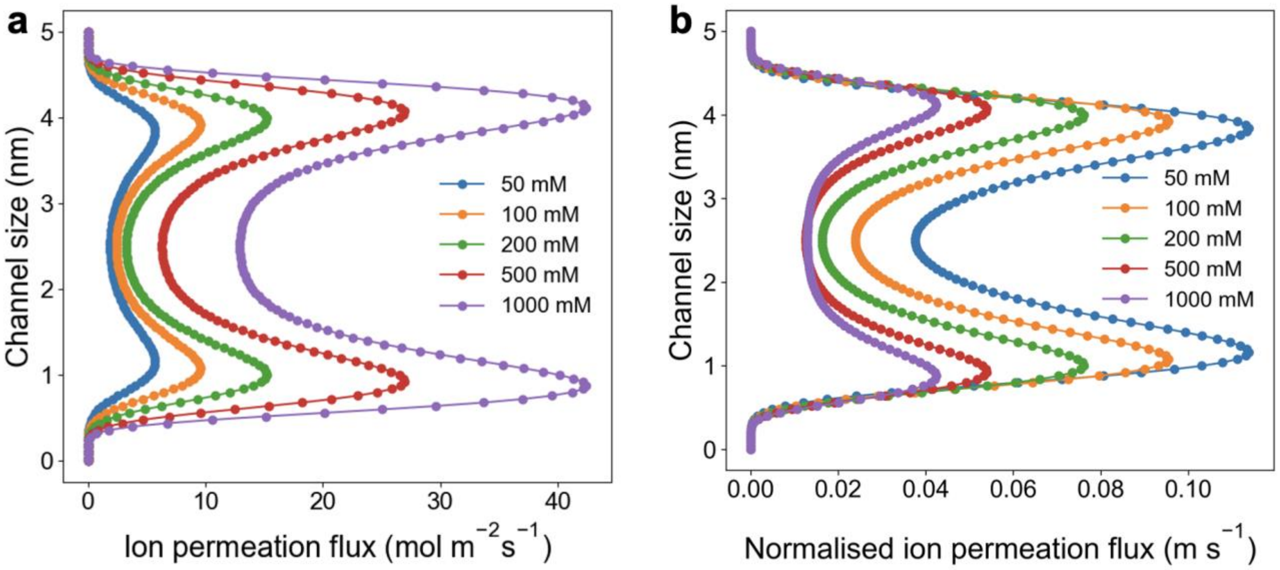

Supplementary Fig. 25 Distribution of ion permeation flux averaged in the lateral direction across the electrified 5 nm channels at the highest charge density. a, Averaged ion permeation flux. **b**, Averaged ion permeation flux normalised by the corresponding feed concentrations. All these results are determined from the results in Supplementary Fig. 23.

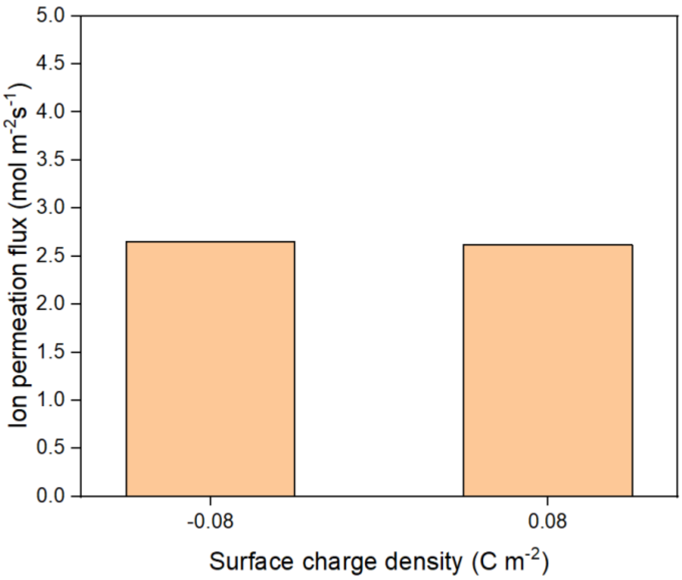

Supplementary Fig. 26 Ion permeation flux in positively and negatively charged nanochannels. All these results were obtained from the IC/PNP models with the channel size of 2 nm and KCl feed concentration of 50 mM.

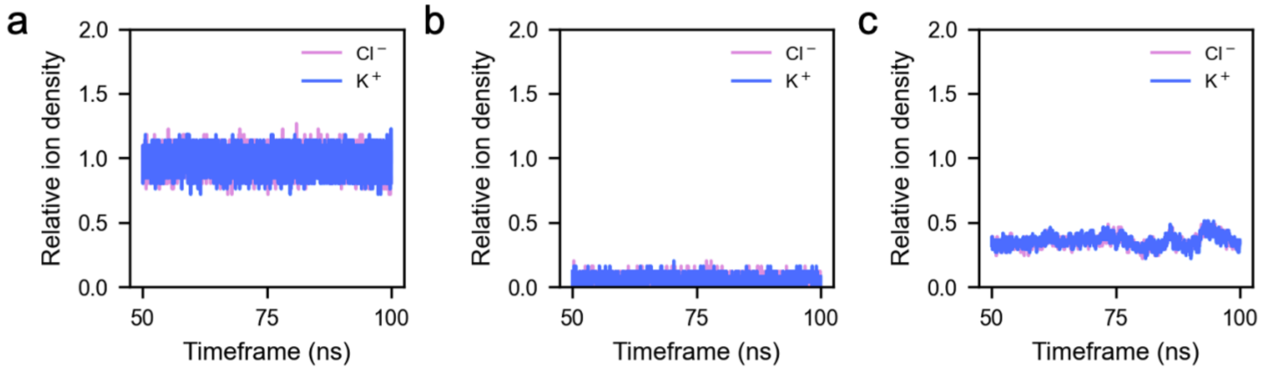

Supplementary Fig. 27 The ion concentrations in the feed, permeate, and graphene channel regions as a function of simulation time in production runs. a-c, Relative ion densities of K^+ (blue) and Cl^- (plum), normalised by their bulk values in a 1000 mM KCl solution, as a function of simulation time over the 50 ns of the production run, corresponding to the steady-state regime: Feed reservoir control region with a target concentration of 1000 mM (**a**); Permeate reservoir control region with a target concentration of 0 mM (**b**); Graphene nanochannel region (**c**). The stable ion concentrations observed in **a** and **b** confirm the effectiveness of the CμMD approach in maintaining prescribed ion concentrations. The plateau in **c** further indicates that a steady-state ion permeation process has been successfully established.

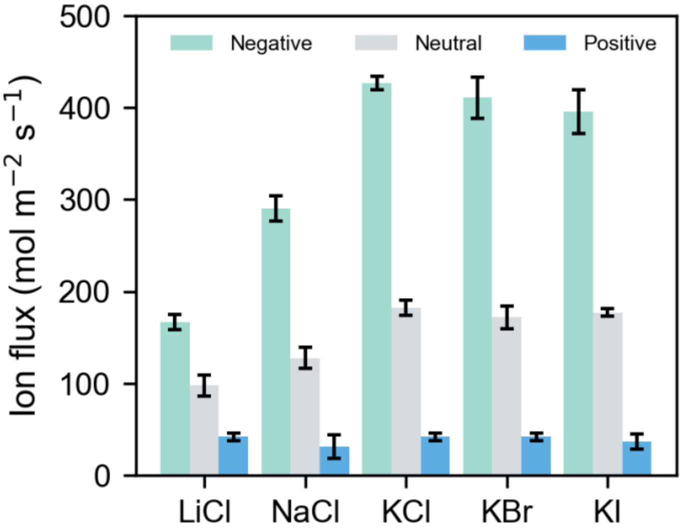

Supplementary Fig. 28 Ion fluxes of different electrolytes through a graphene nanochannel based on MD simulations. Ion fluxes for five electrolyte systems (LiCl, NaCl, KCl, KBr, and KI) are shown under three surface charge conditions: negative (–0.3 C m^{-2}, green), neutral (0 C m^{-2}, grey), and positive (0.3 C m^{-2}, blue). Error bars represent the standard error over three independent 20 ns intervals.

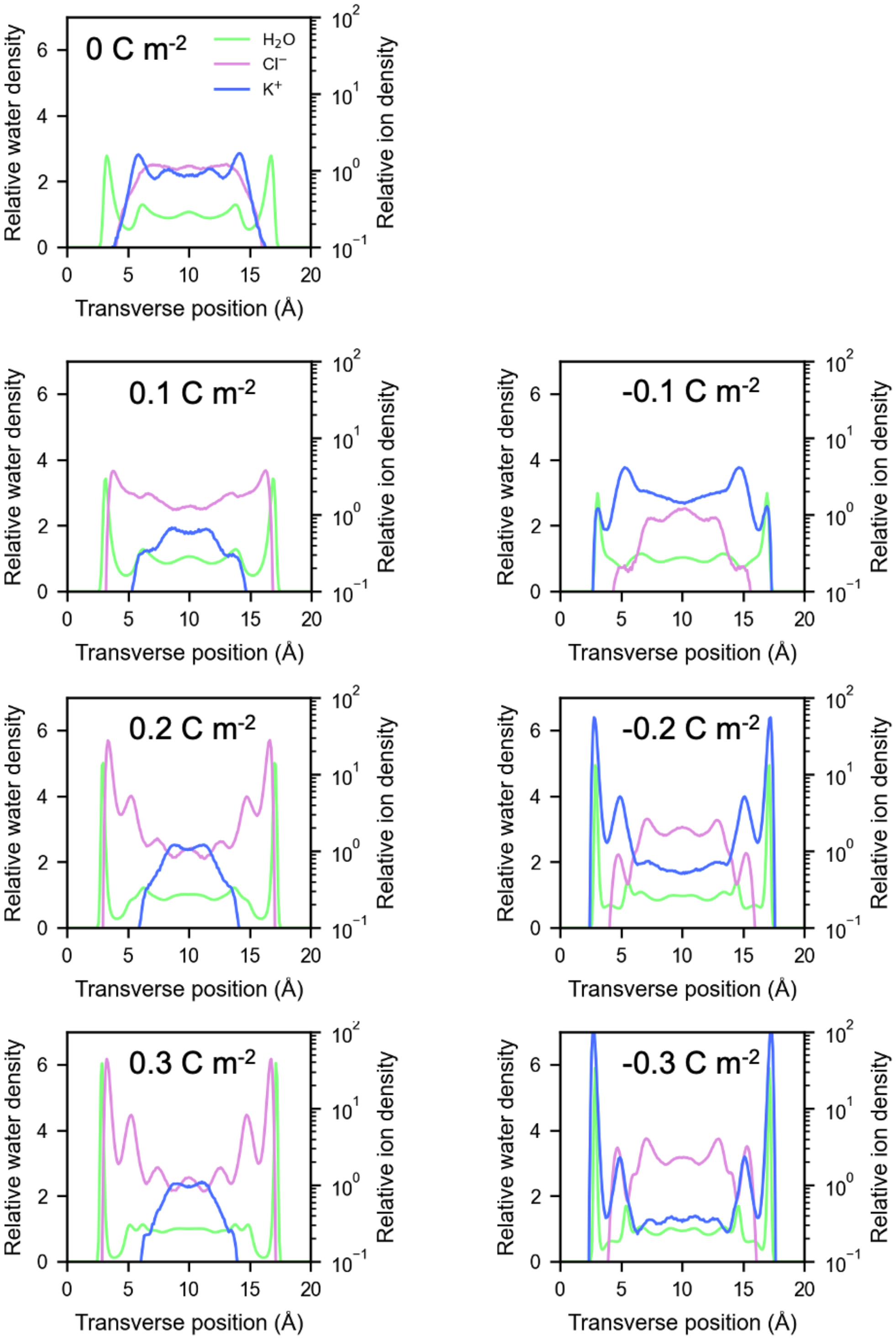

Supplementary Fig. 29 Transverse density profiles of water molecules and ions under varying surface charge densities. Density profiles of water (H_2O, green), K^+ (blue), and Cl^- (plum), normalised by their bulk values in a 1000 mM KCl solution, are shown as a function of the transverse position across the graphene nanochannel at surface charge densities ranging from –0.3 to 0.3 C m^{-2}. The water density was computed based on the oxygen atom distribution, which is taken as the molecular centre of mass.

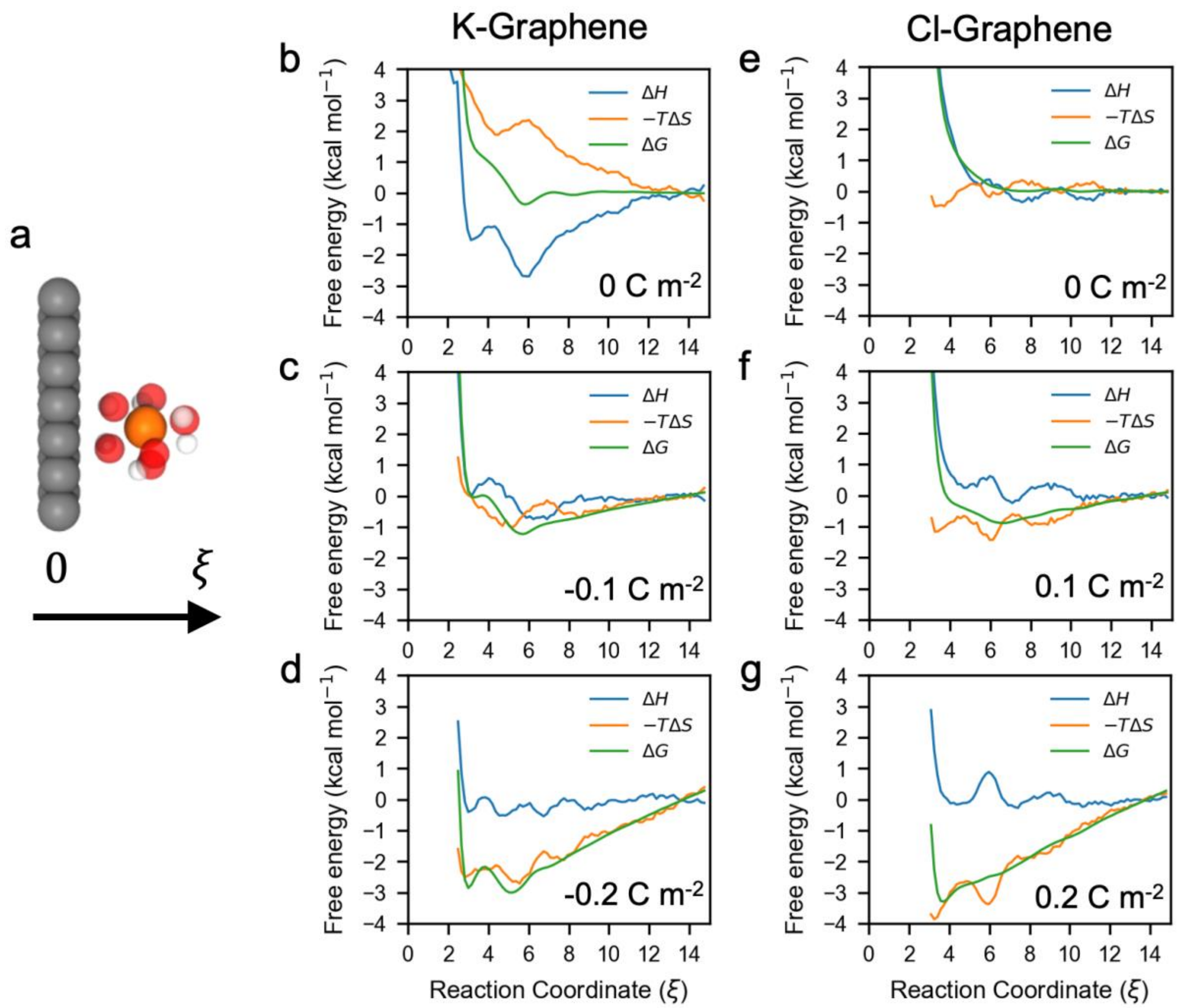

Supplementary Fig. 30 Thermodynamic decomposition of the free energy for ion adsorption at graphene surfaces under different surface charge densities. a, Schematic showing the reaction coordinate starting from graphene surface and proceeds toward the ion's bulk-like position. **b-d**, The free energy profiles of K$^+$ ion approaching a graphene surface along the reaction coordinate under surface charge densities of 0, –0.1, and –0.2 C m^{-2}, respectively. **e-g**, The free energy profiles of Cl$^-$ ion approaching a graphene surface along the reaction coordinate under surface charge densities of 0, –0.1, and –0.2 C m^{-2}, respectively. Each free energy profile is decomposed into enthalpic (ΔH), entropic (–TΔS), and total ($\Delta G = \Delta H - T\Delta S$) contributions as a function of the reaction coordinate (ξ, in the unit of Å), which represents the ion–surface distance.

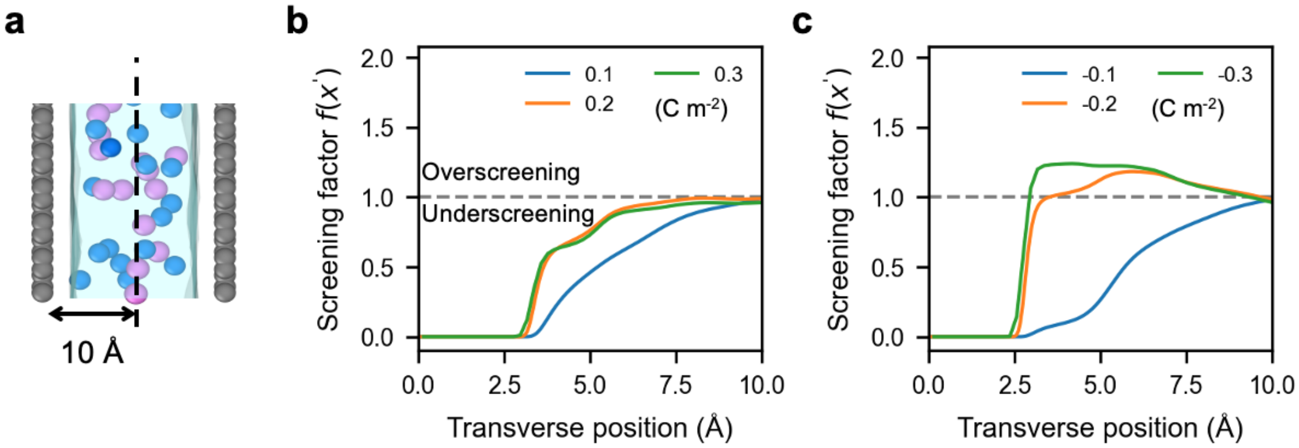

Supplementary Fig. 31 Charge screening behaviour and the emergence of overscreening in charged graphene nanochannels. **a**, Schematic of the transverse cross-section of the graphene slit channel, illustrating the definition of the transverse coordinate used to calculate the screening factor $f'(x) = \int_0^x \frac{F[c_{cation}(x) - c_{anion}(x)]}{|\sigma_s|} dx$, where σ_s is the surface charge and F is the Faraday constant, c_{cation} and c_{anion} are concentration of cation and anion at transverse position x. **b**-**c**, Screening factor profiles $f(x')$ as a function of transverse position for positively (**b**) and negatively (**c**) charged surfaces, under surface charge densities of ±0.1, ±0.2, and ±0.3 C m^{-2}. The screening factor quantifies the ratio of the integrated local ionic charge to the surface charge density. The grey dashed line at $f(x') = 1$ denotes the threshold for perfect screening; values above this indicate overscreening, and values below indicate underscreening.

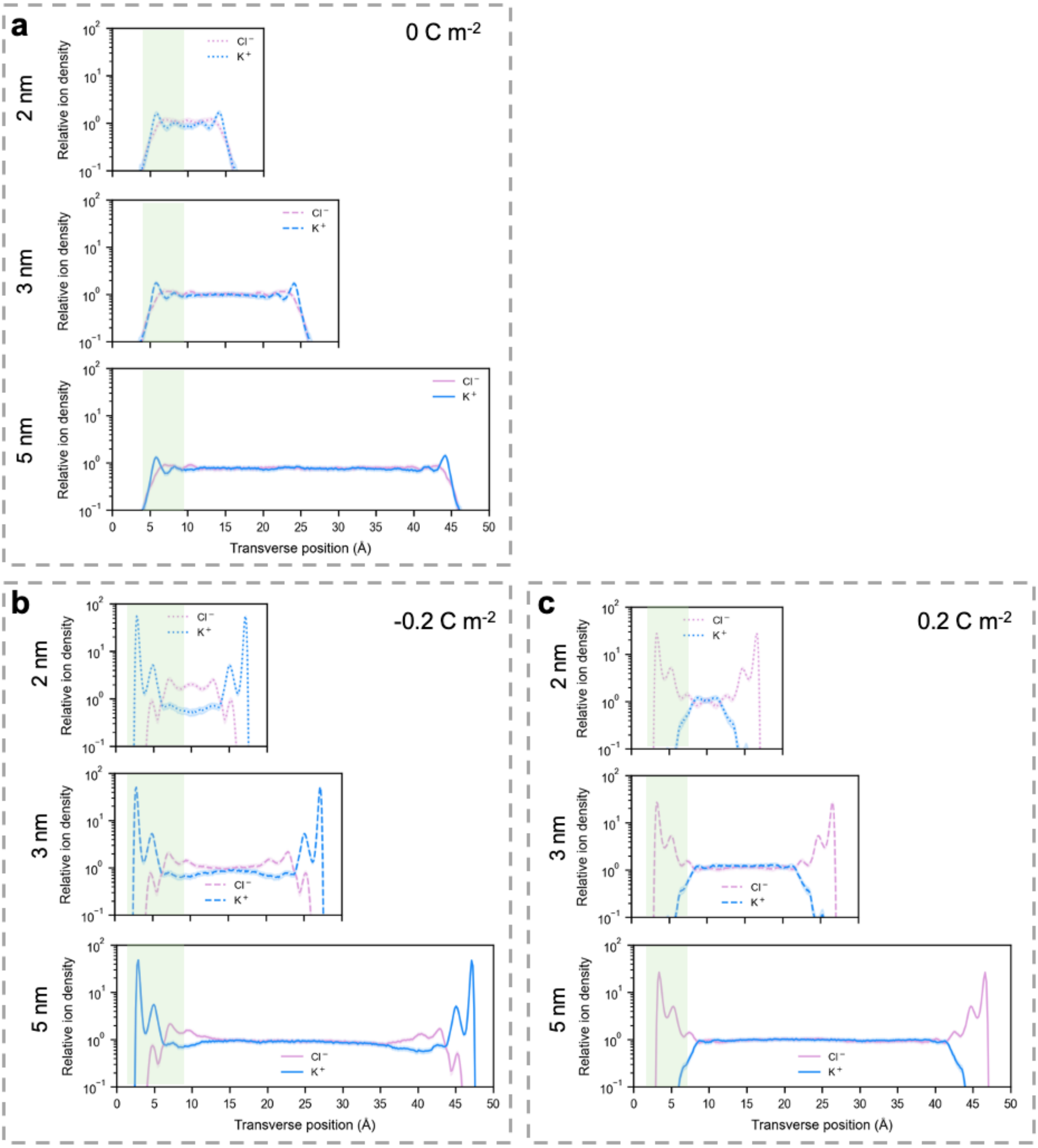

Supplementary Fig. 32 Transverse ion density profiles in charged graphene channels with varying slit sizes. Panels show the transverse distributions of K$^+$ (blue) and Cl$^-$ (plum) ion densities for slit widths of 2, 3, and 5 nm (top to bottom) under three representative surface charge conditions: **a**, neutral (0 C m^{-2}), **b**, negatively charged (–0.2 C m^{-2}), and **c**, positively charged (0.2 C m^{-2}). Notably, across all surface charge conditions, the ion density profiles within the interfacial regions remain nearly invariant with respect to the slit width, as highlighted in light green shade, suggesting ion structures are modulated by interfacial electrostatic interactions rather than spatial nanoconfinement.

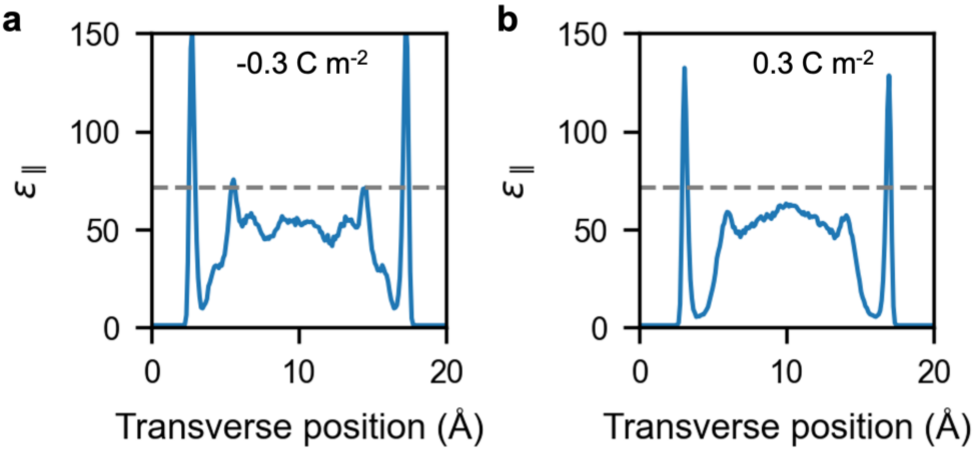

Supplementary Fig. 33 Spatial profiles of in-plane dielectric permittivity of interfacial water in charged graphene nanochannels. a-b, Transverse distributions of the in-plane dielectric permittivity $\varepsilon_{\parallel}$ under negative (–0.3 C m^{-2}, **a**) and positive (0.3 C m^{-2}, **b**) charges. The dielectric permittivity is averaged along the lateral (*z*) direction of the channel from the entrance to the exit. The horizontal dashed line denotes the bulk dielectric constant of SPC/E water (~71).

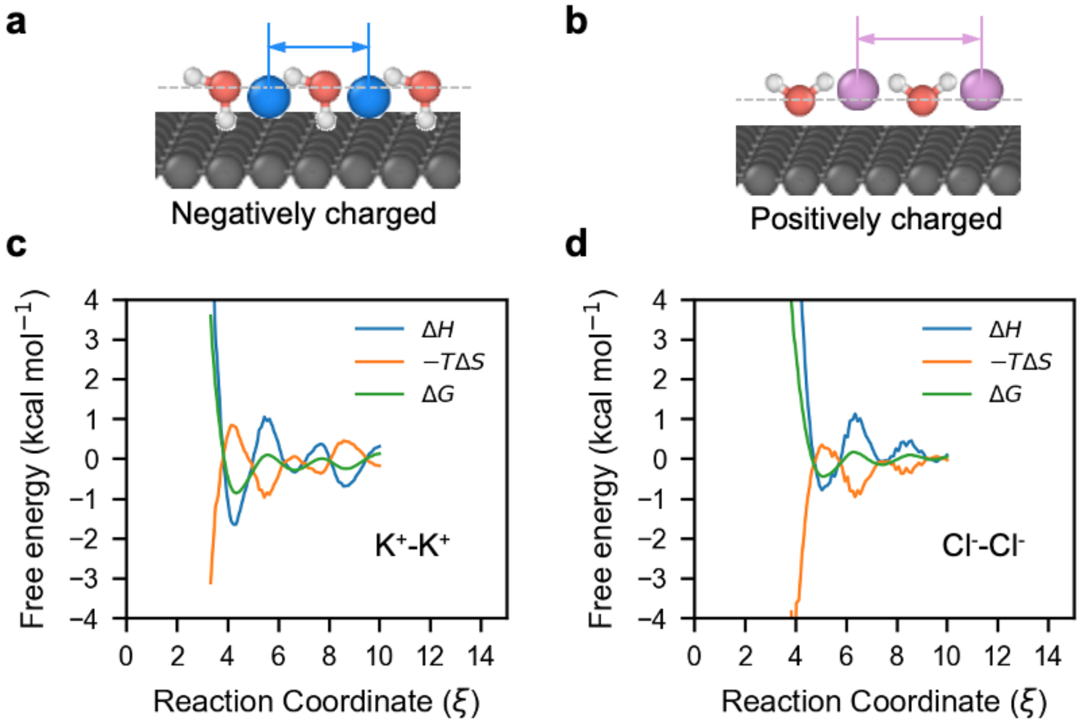

Supplementary Fig. 34 Thermodynamic decomposition of free energy for like-charge ion–ion coupling near charged graphene surfaces. a-b, Schematics illustrating the representative configurations of like-charged ion pairs interacting near negatively and positively charged graphene surfaces, respectively. **c**-**d**, The free energy profiles (ΔG, green) and their decomposition into enthalpic (ΔH, blue) and entropic (−TΔS, orange) contributions for K^+–K^+ pairs near a negatively charged surface (**c**) and Cl^-–Cl^- pairs near a positively charged surface (**d**), as a function of the reaction coordinate ξ, which corresponds to the ion–ion separation distance in the unit of Å. Notably, the first ΔG minima are predominantly driven by favourable enthalpic component (ΔH), highlighting the role of water structuring and thermal fluctuations in stabilizing ion–ion associations.

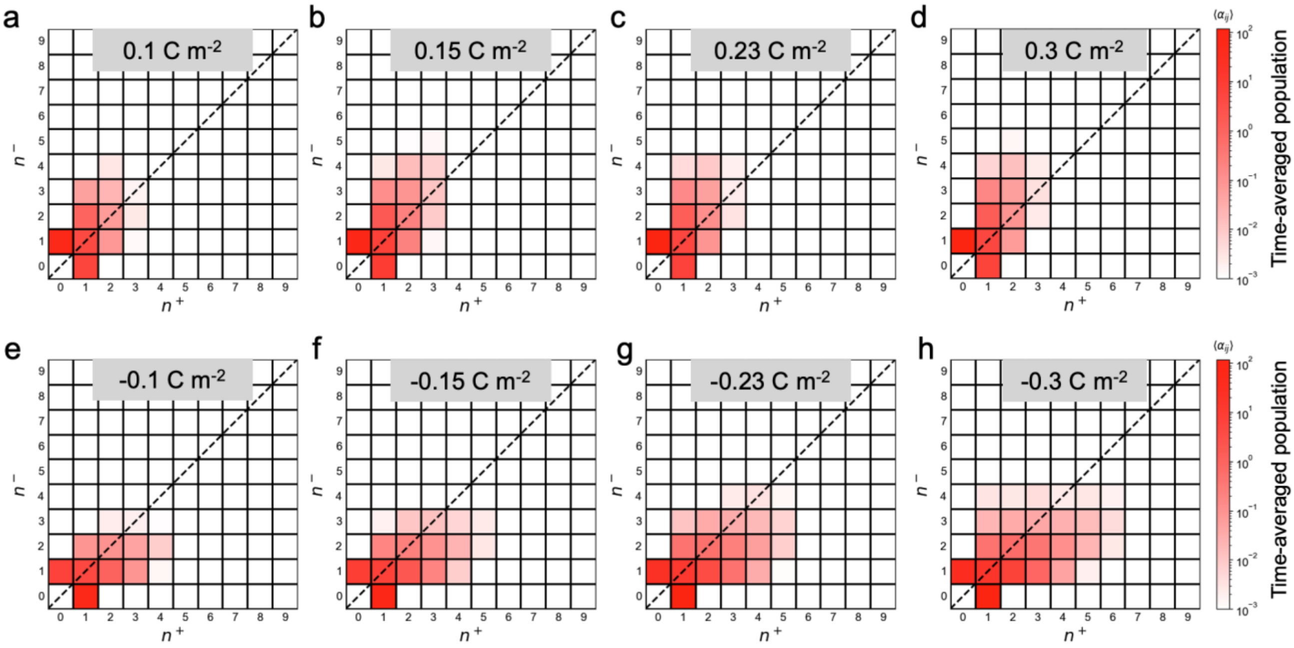

Supplementary Fig. 35 Population statistics of co-ion involved ion cluster in graphene channels with different charge densities. a-h, The cluster size distribution matrices for KCl in graphene nanochannels under surface charge densities ranging from 0.1 to 0.3 C m^{-2} (top row) and –0.1 to –0.3 C m^{-2} (bottom row). n^+ and n^- stand for number of cations and anions in the cluster, respectively. Colour intensity represents the logarithm of the time-averaged population of each cluster type. The diagonal line corresponds to neutral clusters (where $n^+ = n^-$).

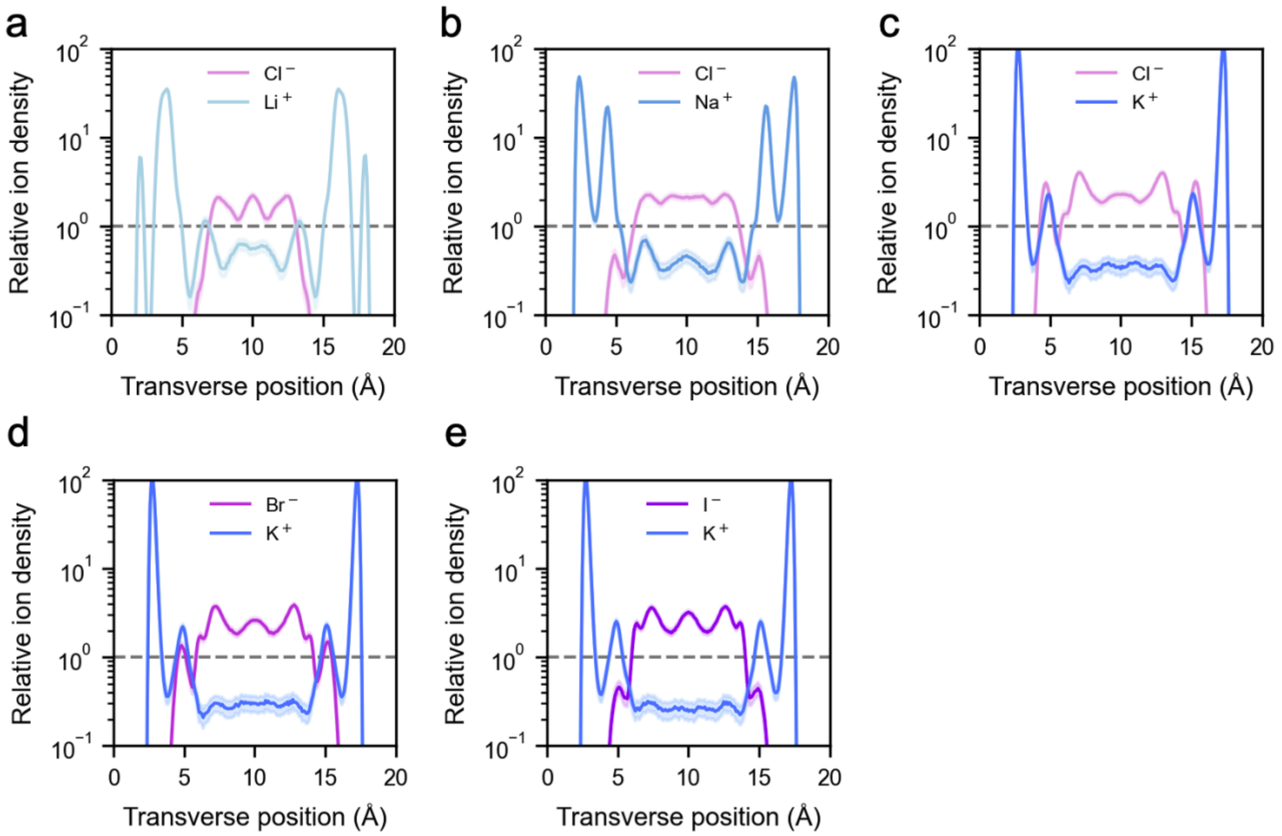

Supplementary Fig. 36 Transverse ion density profiles for different electrolyte systems in negatively charged graphene nanochannels. Density profiles of cations and anions, normalised by their bulk values in a 1000 mM solution, are shown across the transverse direction of the channel. **a-c**, Density profiles of LiCl, NaCl, and KCl, respectively. **d-e**, Density profiles of KBr, and KI, respectively. The grey dashed lines indicate ion density in 1000 mM bulk solution.

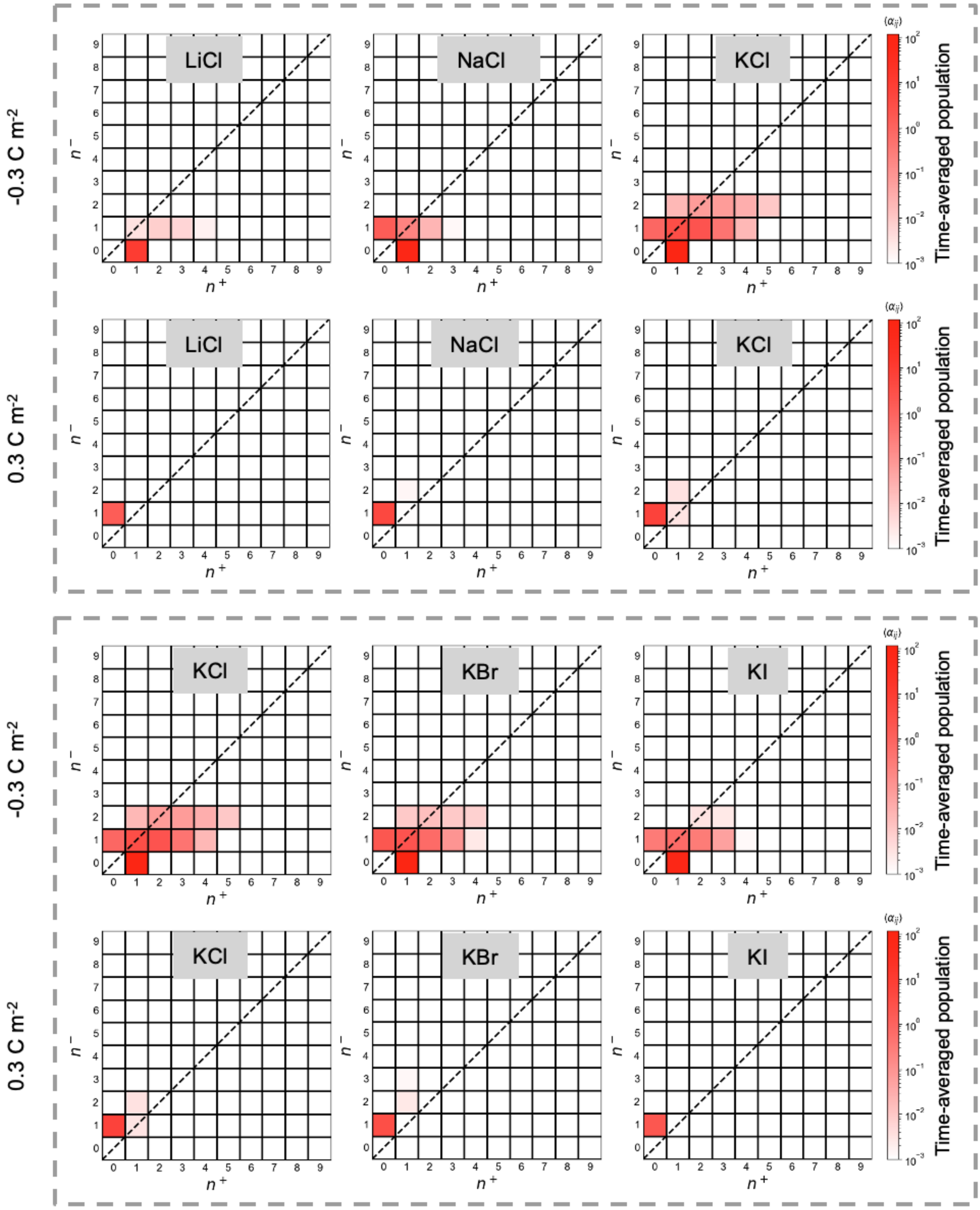

Supplementary Fig. 37 Cluster size distribution matrices for different electrolytes in charged nanochannels. Heatmaps illustrate the probability distributions of ion cluster sizes in the form of two-dimensional matrices, where the *x*- and *y*-axes denote the number of cations (n^{+}) and anions (n^{-}), respectively, in each identified cluster. Colour intensity reflects the time-averaged population of each cluster type, shown on a logarithmic scale. Top two panels show LiCl, NaCl, and KCl electrolytes under surface charge densities of –0.3 C m^{-2} (top row) and 0.3 C m^{-2} (bottom row). Bottom two panels show KCl, KBr, and KI systems under the same surface charge conditions.

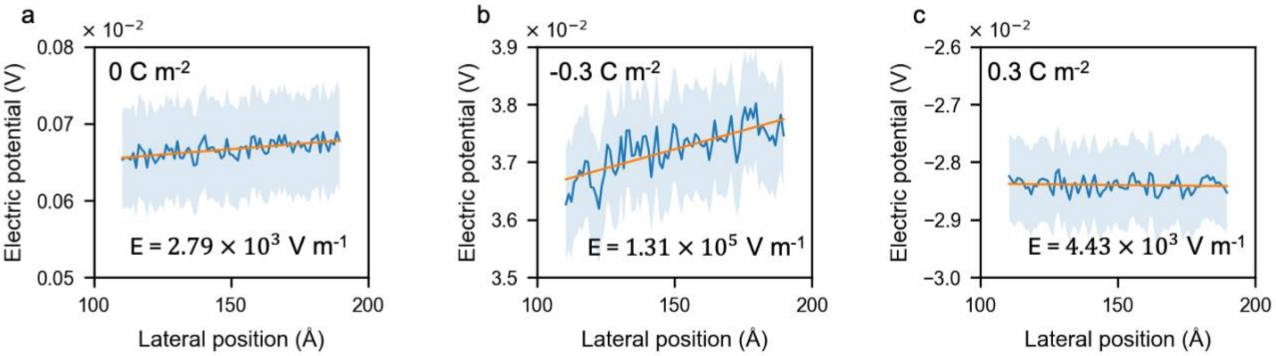

Supplementary Fig. 38 Lateral electric potential profiles and corresponding electric field strength in the graphene nanochannel under different surface charge conditions. a-c, The laterally resolved electric potential across the central region of the graphene channel (from *z* = 110 to 190 Å) for surface charge densities of 0 C m^{-2}, –0.3 C m^{-2}, and 0.3 C m^{-2}, respectively. The blue lines represent the instantaneous electrostatic potential, and the orange lines show the linear fits used to extract the lateral electric field. The resulting electric field strength (*E*) is reported in each panel.

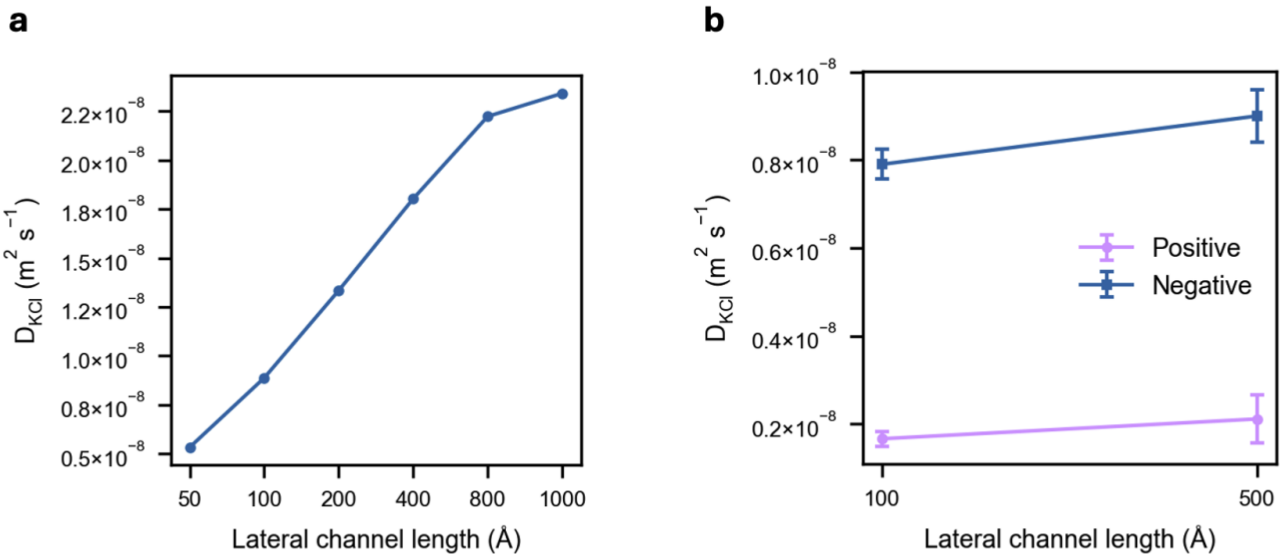

Supplementary Fig. 39 Effect of channel length on the D_{KCl} through electrified graphene nanochannels based on IC/PNP modelling and MD simulations. a, D_{KCl} as a function of channel length ranging from 50 to 1000 nm based on IC/PNP model. All channels have a fixed slit height of 2 nm and are subjected to a surface charge density of –0.09 C m^{-2}, corresponding to a gate voltage of –0.3 V. The feed and permeate concentrations are set to 50 mM and 10^{-2} mM, respectively. **b**, D_{KCl} as a function of channel length ranging from 100 to 500 Å in MD simulations. All channels have a fixed slit height of 2 nm and are subjected to a surface charge density of –0.2 C m^{-2}. The feed KCl concentration is 1000 mM and permeate concentration is 0 mM. These results in both continuum modelling and MD simulations show that D_{KCl} further increases with the channel length, indicating that the interfacial enhancement of ion transport becomes more prominent in larger systems. Notably, the channel lengths considered in above multiscale modellings is still far shorter than the millimetre-scale membrane length used in experiments, making the incomparable D_{KCl} between modelling and experiments.

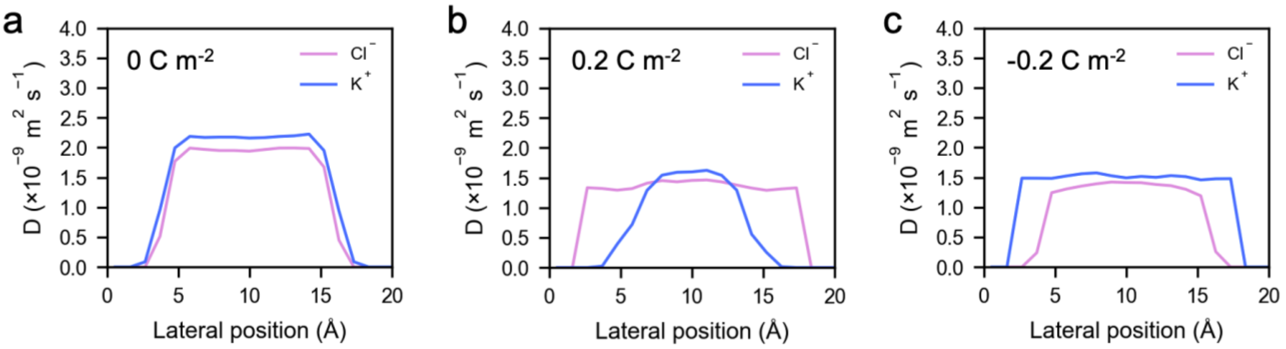

Supplementary Fig. 40 Position-dependent lateral diffusivity of K^+ and Cl^- ions in graphene nanochannels under different surface charge conditions. a-c, show the local lateral diffusion coefficients D of K^+ (blue) and Cl^- (plum) ions as a function of position along the transverse direction of the nanochannel for surface charge densities of 0 C m^{-2} (**a**), 0.2 C m^{-2} (**b**), and –0.2 C m^{-2} C m^{-2} (**c**).

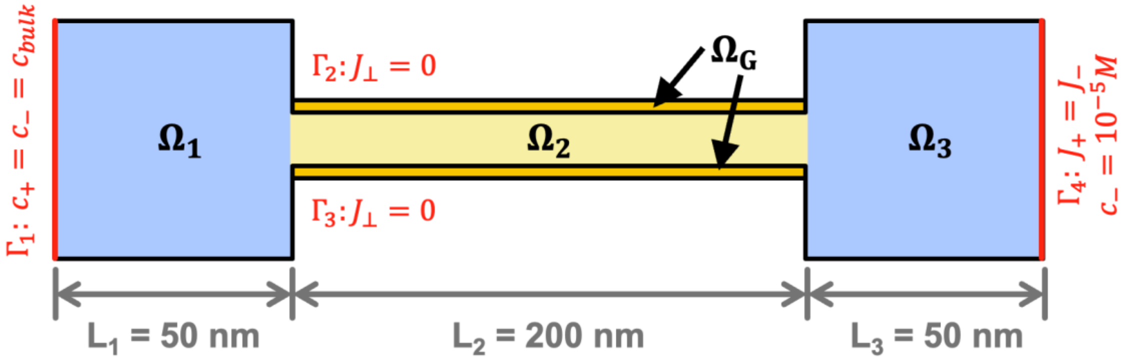

Supplementary Fig. 41 The geometry and boundary conditions of the nanochannel model used for continuum modelling. A rescaled geometry of the model was shown, where the feed (**Ω_1**) and permeate (**Ω_3**) reservoirs (squared, $L_1 = L_3 = 50$ nm) are connected by a single nanoslit (**Ω_3**), in-plane length of $L_2 = 200$ nm). Graphene sheets were denoted as **Ω_G**. To study the ion flow at an equilibrium state, boundary conditions **Γ_1** and **Γ_4** are applied to maintain a constant concentration difference between feed and permeate reservoirs.

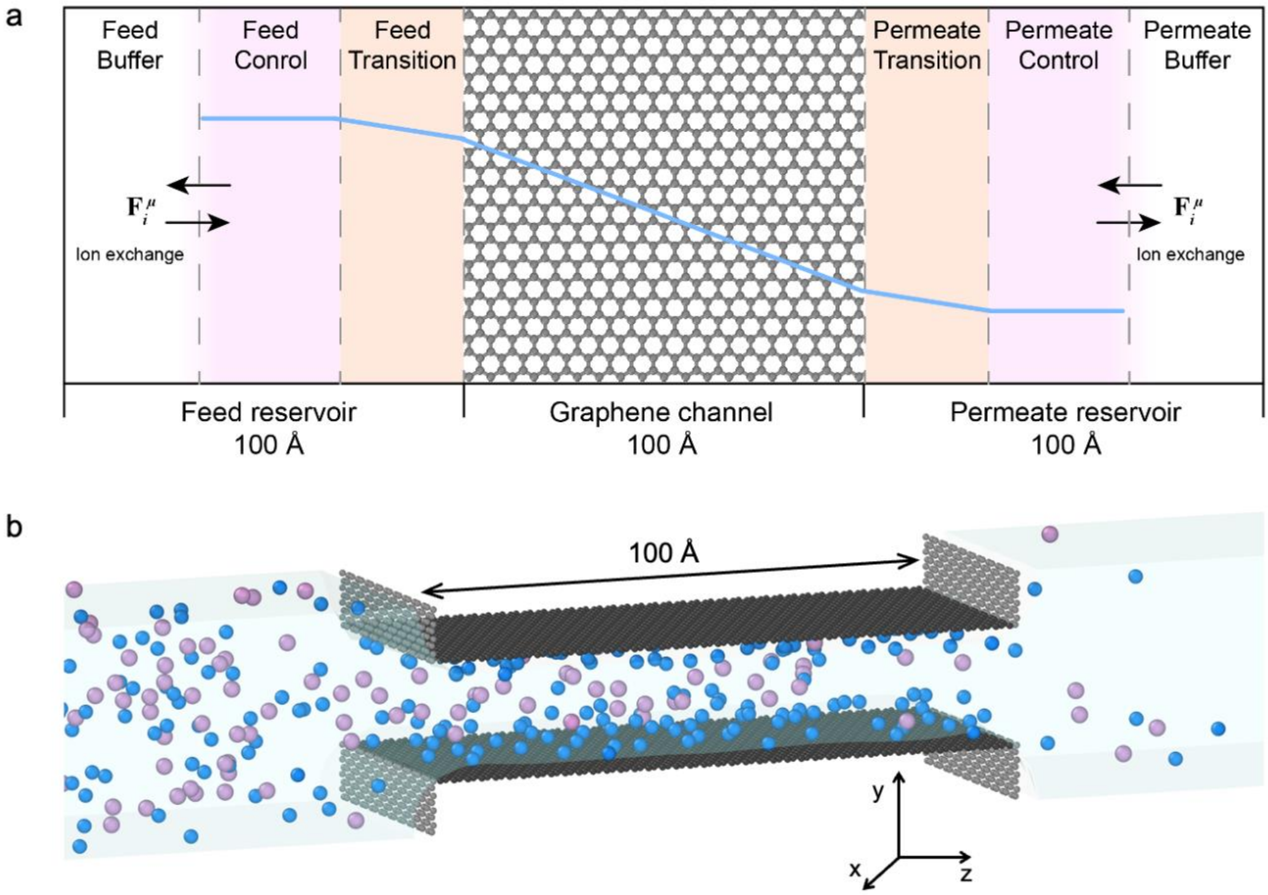

Supplementary Fig. 42 Schematic of the MD simulation system and constant chemical potential molecular dynamics (CμMD) setup. a, The CμMD system consists of a feed reservoir, a graphene slit nanochannel, and a permeate reservoir, aligned along the *z*-axis. The control regions (shaded in light plum) are located at the feed and permeate sides of the simulation box and are coupled to adjacent buffer regions to regulate ion concentrations via constraint forces. Transition regions (shaded in red) connect the control regions and the channel to avoid artificial perturbations. The graphene channel wall is modelled using two parallel graphene sheets. The blue line illustrates a representative ion concentration profile across the system under steady-state conditions. **b**, The MD simulation system comprises a feed reservoir (left), a graphene slit nanochannel (centre), and a permeate reservoir (right). Two parallel graphene sheets form the channel walls (black), while additional neutral graphene sheets (grey) are used to cap the channel entrances, creating a single-slit geometry. Water molecules are represented as transparent medium for clarity. Blue and plum spheres represent cations and anions, respectively, illustrating the establishment of a concentration gradient across the channel. The coordinate axes denote the spatial orientation of the simulation box, with ion transport occurring along the *z*-direction.

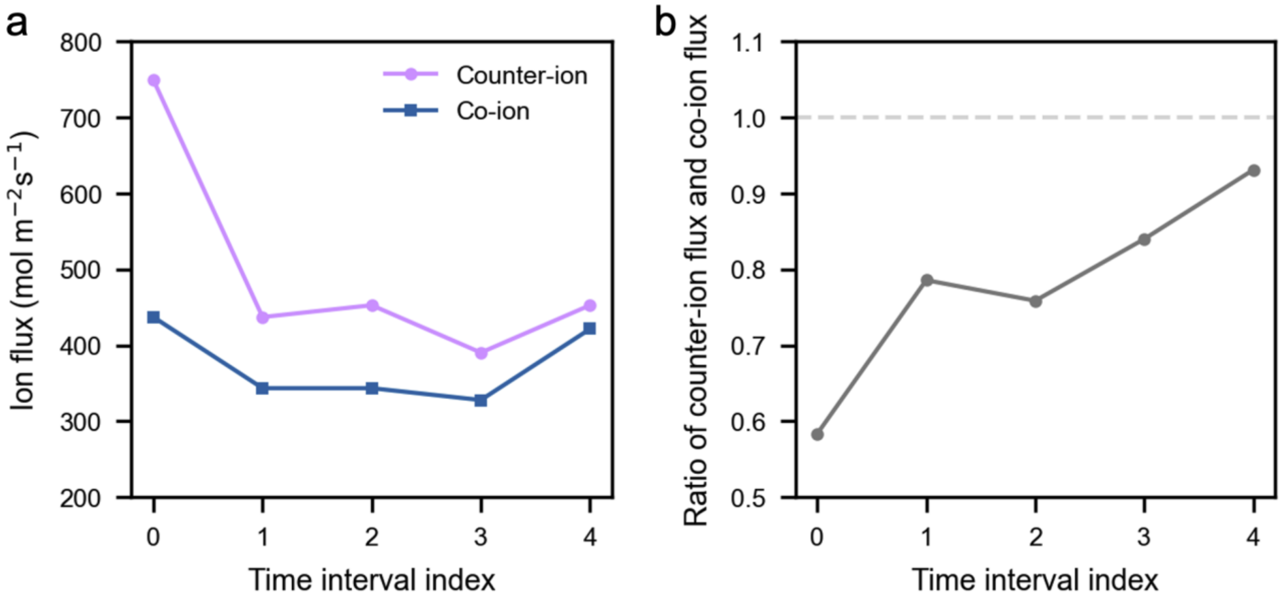

Supplementary Fig. 43 Temporal evolution of cation and anion permeation flux under variable constraint on K^+ ions in permeate reservoir. **a**, The cation and anion permeation flux across the channel at five different 20 ns time intervals. **b**, The ratio of cation and anion flux in **a**, the dashed line illustrates the ratio of 1, indicating the cation and anion flux ratio is approaching 1.

References

1. Stein, D., Kruithof, M. & Dekker, C. Surface-charge-governed ion transport in nanofluidic channels. *Phys. Rev. Lett.* **93**, 035901 (2004).
2. Schoch, R. B., Han, J. & Renaud, P. Transport phenomena in nanofluidics. *Rev. Modern Phys.* **80**, 839–883 (2008).
3. Bocquet, L. & Charlaix, E. Nanofluidics, from bulk to interfaces. *Chem. Soc. Rev.* **39**, 1073–95 (2010).
4. Duan, C. & Majumdar, A. Anomalous ion transport in 2-nm hydrophilic nanochannels. *Nat. Nanotechnol.* **5**, 848–852 (2010).
5. Tunuguntla, R. H., Henley, R. Y., Yao, Y.-C., Pham, T. A., Wanunu, M. & Noy, A. Enhanced water permeability and tunable ion selectivity in subnanometer carbon nanotube porins. *Science* **357**, 792–796 (2017).
6. Esfandiar, A., Radha, B., Wang, F. C., Yang, Q., Hu, S., Garaj, S., Nair, R. R., Geim, A. K. & Gopinadhan, K. Size effect in ion transport through angstrom-scale slits. *Science* **358**, 511–513 (2017).
7. Gopinadhan, K., Hu, S., Esfandiar, A., Lozada-Hidalgo, M., Wang, F. C., Yang, Q., Tyurnina, A. V., Keerthi, A., Radha, B. & Geim, A. K. Complete steric exclusion of ions and proton transport through confined monolayer water. *Science* **363**, 145–148 (2019).
8. Faucher, S., Aluru, N., Bazant, M. Z., Blankschtein, D., Brozena, A. H., Cumings, J., Pedro de Souza, J., Elimelech, M., Epsztein, R., Fourkas, J. T., Rajan, A. G., Kulik, H. J., Levy, A., Majumdar, A., Martin, C., McEldrew, M., Misra, R. P., Noy, A., Pham, T. A., *et al.* Critical Knowledge Gaps in Mass Transport through Single-Digit Nanopores: A Review and Perspective. *J. Phys. Chem. C* **123**, 21309–21326 (2019).
9. Bocquet, L. Nanofluidics coming of age. *Nat. Mater.* **19**, 254–256 (2020).
10. Zhang, Z., Wen, L. & Jiang, L. Nanofluidics for osmotic energy conversion. *Nat. Rev. Mater.* **6**, 622–639 (2021).
11. Kavokine, N., Netz, R. R. & Bocquet, L. Fluids at the Nanoscale: From Continuum to Subcontinuum Transport. *Annu. Rev. Fluid Mech.* **53**, 377–410 (2021).
12. Emmerich, T., Vasu, K. S., Niguès, A., Keerthi, A., Radha, B., Siria, A. & Bocquet, L. Enhanced nanofluidic transport in activated carbon nanoconduits. *Nat. Mater.* **21**, 696–702 (2022).
13. You, Y., Ismail, A., Nam, G.-H., Goutham, S., Keerthi, A. & Radha, B. Angstrofluidics: Walking to the Limit. *Annu. Rev. Mater. Res.* **52**, 189–218 (2022).
14. Aluru, N. R., Aydin, F., Bazant, M. Z., Blankschtein, D., Brozena, A. H., de Souza, J. P., Elimelech, M., Faucher, S., Fourkas, J. T., Koman, V. B., Kuehne, M., Kulik, H. J., Li, H.-K., Li, Y., Li, Z., Majumdar, A., Martis, J., Misra, R. P., Noy, A., *et al.* Fluids and Electrolytes under Confinement in Single-Digit Nanopores. *Chem. Rev.* **123**, 2737–2831 (2023).
15. Emmerich, T., Ronceray, N., Agrawal, K. V., Garaj, S., Kumar, M., Noy, A. & Radenovic, A. Nanofluidics. *Nat. Rev. Methods Primers* **4**, 1–18 (2024).
16. Li, Z., Misra, R. P., Li, Y., Yao, Y.-C., Zhao, S., Zhang, Y., Chen, Y., Blankschtein, D. & Noy, A. Breakdown of the nernst–einstein relation in carbon nanotube porins. *Nat. Nanotechnol.* **18**, 177–183 (2022).
17. English, N. J. & Waldron, C. J. Perspectives on external electric fields in molecular simulation: progress, prospects and challenges. *Phys. Chem. Chem. Phys.* **17**, 12407–12440 (2015).
18. Berthoumieux, H., Démery, V. & Maggs, A. C. Nonlinear conductivity of aqueous electrolytes: Beyond the first Wien effect. *J. Chem. Phys.* **161**, 184504 (2024).
19. Wu, J. Understanding the Electric Double-Layer Structure, Capacitance, and Charging Dynamics. *Chem. Rev.* **122**, 10821–10859 (2022).

20. Gonella, G., Backus, E. H. G., Nagata, Y., Bonthuis, D. J., Loche, P., Schlaich, A., Netz, R. R., Kühnle, A., McCrum, I. T., Koper, M. T. M., Wolf, M., Winter, B., Meijer, G., Campen, R. K. & Bonn, M. Water at charged interfaces. *Nat. Rev. Chem.* **5**, 466–485 (2021).
21. Bazant, M. Z., Storey, B. D. & Kornyshev, A. A. Double Layer in Ionic Liquids: Overscreening versus Crowding. *Phys. Rev. Lett.* **106**, 046102 (2011).
22. Lee, S. S., Koishi, A., Bourg, I. C. & Fenter, P. Ion correlations drive charge overscreening and heterogeneous nucleation at solid–aqueous electrolyte interfaces. *Proc. Natl. Acad. Sci.* **118**, e2105154118 (2021).
23. Tian, Y., Song, Y., Xia, Y., Hong, J., Huang, Y., Ma, R., You, S., Guan, D., Cao, D., Zhao, M., Chen, J., Song, C., Liu, K., Xu, L.-M., Gao, Y. Q., Wang, E.-G. & Jiang, Y. Nanoscale one-dimensional close packing of interfacial alkali ions driven by water-mediated attraction. *Nat. Nanotechnol.* **19**, 479–484 (2024).
24. Xu, K. *Electrolytes, Interfaces and Interphases*. (The Royal Society of Chemistry, 2023). doi:10.1039/9781837671311.
25. France-Lanord, A. & Grossman, J. C. Correlations from Ion Pairing and the Nernst-Einstein Equation. *Phys. Rev. Lett.* **122**, 136001 (2019).
26. Dočkal, J., Moučka, F. & Lísal, M. Molecular Dynamics of Graphene–Electrolyte Interface: Interfacial Solution Structure and Molecular Diffusion. *J. Phys. Chem. C* **123**, 26379–26396 (2019).
27. Xue, Y., Xia, Y., Yang, S., Alsaid, Y., Fong, K. Y., Wang, Y. & Zhang, X. Atomic-scale ion transistor with ultrahigh diffusivity. *Science* **372**, 501–503 (2021).
28. Wang, Y., Tang, F., Yu, X., Chiang, K.-Y., Yu, C.-C., Ohto, T., Chen, Y., Nagata, Y. & Bonn, M. Interfaces govern the structure of angstrom-scale confined water solutions. *Nat Commun* **16**, 7288 (2025).
29. Steinmann, S. N. & Seh, Z. W. Understanding electrified interfaces. *Nat. Rev. Mater.* **6**, 289–291 (2021).
30. Kilic, M. S., Bazant, M. Z. & Ajdari, A. Steric effects in the dynamics of electrolytes at large applied voltages. I. Double-layer charging. *Phys. Rev. E* **75**, 021502 (2007).
31. Storey, B. D. & Bazant, M. Z. Effects of electrostatic correlations on electrokinetic phenomena. *Phys. Rev. E* **86**, 056303 (2012).
32. Cheng, C., Jiang, G., Simon, G. P., Liu, J. Z. & Li, D. Low-voltage electrostatic modulation of ion diffusion through layered graphene-based nanoporous membranes. *Nat. Nanotechnol.* **13**, 685–690 (2018).